Multiscale study of enhancing the fracture properties of interfacial transition zone: insights from molecular dynamics and finite element simulations

Benzhi Min[a], Xi Chen[b], Ke Li[c], Zhenqing Wang[a,*]

[a]*College of Aerospace and Civil Engineering, Harbin Engineering University, Harbin, 150001, China*
[b]*Nanyang Technological University, School of Materials Science and Engineering, Singapore, 639798, Republic of Singapore*
[c]*Institute of Materials Research and Engineering (IMRE), Agency for Science, Technology and Research (A*STAR) , 2 Fusionopolis Way, Innovis #08-03, Singapore, 138634, Republic of Singapore*

Abstract

Cementitious composites are widely used in architecture and construction field, but usually show quasi-brittle failure at macroscale under tensile or bending loads. In contrast, the calcium silicate hydrates (C-S-H) exhibits noticeable ductile response at nanoscale. In this article, we focus on the interfacial transition zone between cement paste and aggregate, which consists of the C-S-H/quartz and the calcium hydroxide (CH)/quartz interface structures. To comprehend how a nanoscale design might improve concrete's macro mechanical qualities, molecular dynamics and finite element simulations are performed at the nanoscale and macroscale, respectively. The elastic properties, modulus, fracture toughness and critical energy release rate of C-S-H/CH/graphene oxide (GO)/quartz composites are calculated using the molecular dynamics method at nanoscale. These parameters then are used in macro-simulation and calculating mechanical properties of macro concrete structures. The incorporation of GO sheets into the interface results in a 38.40% to 58.06% increase in the fracture toughness of interfacial transition zone (ITZ) systems and an 80% and 9.81% improvement in the tensile strength and tensile modulus of the concrete model, respectively. This fundamental insight into nanoscale interfaces notably allows for more accurate predictions of macroscopic

*correspondingauthor
Email address: wangzhenqing@hrbeu.edu.cn (Zhenqing Wang)

mechanical behavior, paving the way for innovative and enhanced cement-based materials in the future.

Keywords: Calcium silicate hydrate, Multiscale modeling, Interfacial transition zone, Fracture toughness

1. Introduction

Concrete is consumed far more than any other construction material in the word [1], following water. The production of cement clinker consumes large amounts of energy and emit CO_2, with most of the emissions occurring during the calcinations of limestone, which involves the conversion of $CaCO_3$ to CaO. By 2050, there will be a 4682 Mt global demand for commercial concrete, and 2543 Mt of CO_2 will be emitted during the corresponding production process [2]. Reducing CO_2 emissions will be possible, by using a mechanism-based approach at the material community to improve understanding the mechanisms that underpin cement manufacture, concrete curing, and durability [3]. Concrete is well known for its low tensile strength, low durability, quasi-brittle damage, poor deformation performance and multiple cracking behavior [4, 5, 6]. At the microscopic level, it is essential to comprehend how the good ductile damage behavior of C-S-H can lead to quasi-brittle damage behavior of macroscopic concrete. This microscopic understanding will help us to develop tougher and more durable concrete materials at the microscopic level.

Concrete is a multi-component, multi-phase and multi-scale composite material [7]. The structural integrity and load-bearing capacity are typically affected by cracks in concrete, substantially jeopardizing the safety, usability, and durability [8]. There has been lots of research on strengthening the toughness of concrete throughout the past few decades [9, 10], various fibers and nano additives have been reported as efficient concrete modifying agents. Concrete's tensile strength can be increased by steel fibers and polypropylene fibers by 47% and 22%, respectively. [11, 12, 13]. Short carbon, glass and steel fibers with different volume contents significantly increased the first crack stress, fracture energy and toughness [14, 15, 16], decreased the crack width and changed the shape of the crack path from linear pattern to curved form [17]. Fiber bridging, fiber pullout, and fiber fracture are the three basic reinforcement mechanisms of fiber reinforced concrete, which significantly affect the flexural and fracture properties of concrete by bridging the cracks and inhibiting propagation [18]. However, the addition of fiber will lead to a decrease in the mechanical properties if the fiber deforma-

tion are incompatible with matrix, and ITZ in the concrete is not enhanced [19]. Nano additives that can improve the microstructure and mechanical properties of ITZ therefore are highly favored by researchers [20, 21, 22]. Via whisker pull-out, crack deflection, whisker bridging, and whisker fracture, micro-size $CaCO_3$ whiskers effectively inhibited and delayed the generation, extension and coalescence of microcracks [23, 24]. Due to the improved bond strength produced by the incorporation of silica fume, adding more silica fume ($> 20\%$) contributed better to improving the fracture resistance and flexural strength of concrete than steel fiber [25]. ITZ's porosity was significantly reduced by adding GO, which also enhanced the structural morphology of the hydration products, increased the homogenization of the microstructure, and thus increased the micro fracture toughness of ITZ by 24.9% [26, 27]. Carbon nanotubes [28, 29, 30, 31] and nanoscale cellulose filaments [32] can be well dispersed and embedded in the cement hydration products, this mesh-like distribution provides good bonding ability by bridging the pores and decreasing the pore size. The filling effect of nano silica can lengthen the C-S-H gels' chains in ITZ, making the structure denser and optimizing the enhancement of mortar's fracture qualities [33, 34]. The synergistic mechanism of suppressing cracks at different scales brought by the addition of nanomaterials results in higher strength and significant fracture toughness of the cement-based composites [35]. It is clear that ITZ has the most important impact on the toughening of concrete. Understanding the interaction between additives and concrete is more difficult due to the load transmission through adhesion, cementitious material damage, as well as the plastic deformation [36]. Understanding and predicting concrete properties by modeling and simulation methods has become a pursuit of many researchers. In recent years, a variety of concrete fracture models have been developed at different scales [37, 38, 39, 40, 41], however, to simplify calculation, the models are usually applicable to a single scale (e.g. mesoscale), or simplified assumptions are made for constitutive relation at the element level. Existing multiscale models [42, 43, 44, 45] are rarely allowed to take the effects of various nanoadditives on the mechanical properties of concrete into consideration, especially fracture properties at the molecular level. Therefore, a multiscale model that allows the consideration of different types of nanoadditives, and focuses on the effect of ITZ on the overall mechanical and fracture properties of concrete, is necessary to help us better understand the effect of micro-component design on concrete properties, with the aim of reducing concrete consumption or extending the service life of concrete buildings.

In this article, we tried to construct a multiscale model for cementitious composites by molecular dynamics (MD) and finite element method (FEM). The inter-

action of the C-S-H/GO/quartz and CH/GO/quartz interface systems were studied using the molecular dynamics method, the radial distribution function (RDF), hydrogen bonds, fracture toughness and energy release rate were analyzed to characterize the fracture behavior of different phase at nanoscale. The MD simulations help us comprehend the mechanism of GO toughening ITZ and provide a series of parameters for fracture properties. These key parameters allow us to construct a finite element model to predict how the interaction between the cement matrix and aggregates affects the concrete's overall fracture properties. The models utilized in this study provide a detailed understanding of how nanoscale design strategies have the potential to augment the macroscopic mechanical properties of concrete materials. This lays the groundwork for the advancement and refinement of cement-based materials in the future.

2. Materials and methods

In this study, we focused on the interfacial transition zone (ITZ) between cement paste and aggregate, the weakest part of concrete. The C-S-H/quartz and CH/quartz interface structures are chosen as the two fundamental structures of ITZ, since C-S-H and CH are the two main products in ITZ. To comprehend how a nanoscale design might improve concrete's macro mechanical qualities, molecular dynamics models and finite element models were developed at the nanoscale and millimeter scale, respectively.

2.1. Molecular dynamics model

2.1.1. Model construction

Fig. 1 shows the main parts of the interfacial transition zone structures: amorphous C-S-H layers, CH, GO sheets, and quartz. The typical structure of tobermorite-11 Å (Hamid) [46] ($a/2 = 5.58$ Å$, b = 7.39$ Å$, c/2 = 11.389$ Å) was used to create the atomic structure of the C-S-H crystal. Previous studies have demonstrated that under various mix proportions and curing processes, the average Ca/Si ratio of C-S-H gel in ordinary cement paste ranges from 1.2 to 2.3 [47] with a mean of 1.75, which is consistent with the nuclear magnetic resonance (NMR) results [48]. In order to keep the C/S ratio around 1.7, large numbers of SiO_2 groups were randomly removed from silicate tetrahedron chains. The final C-S-H structure contains monomers, dimers, pentamers and even octamers with $Q^0 = 10\%$, $Q^1 = 68\%$ and $Q^2 = 22\%$ respectively. Then the Grand Canonical Monte Carlo (GCMC) simulation was carried out to adsorb water molecules. After the reaction between water and Ca SiO_4 groups, we obtained the final

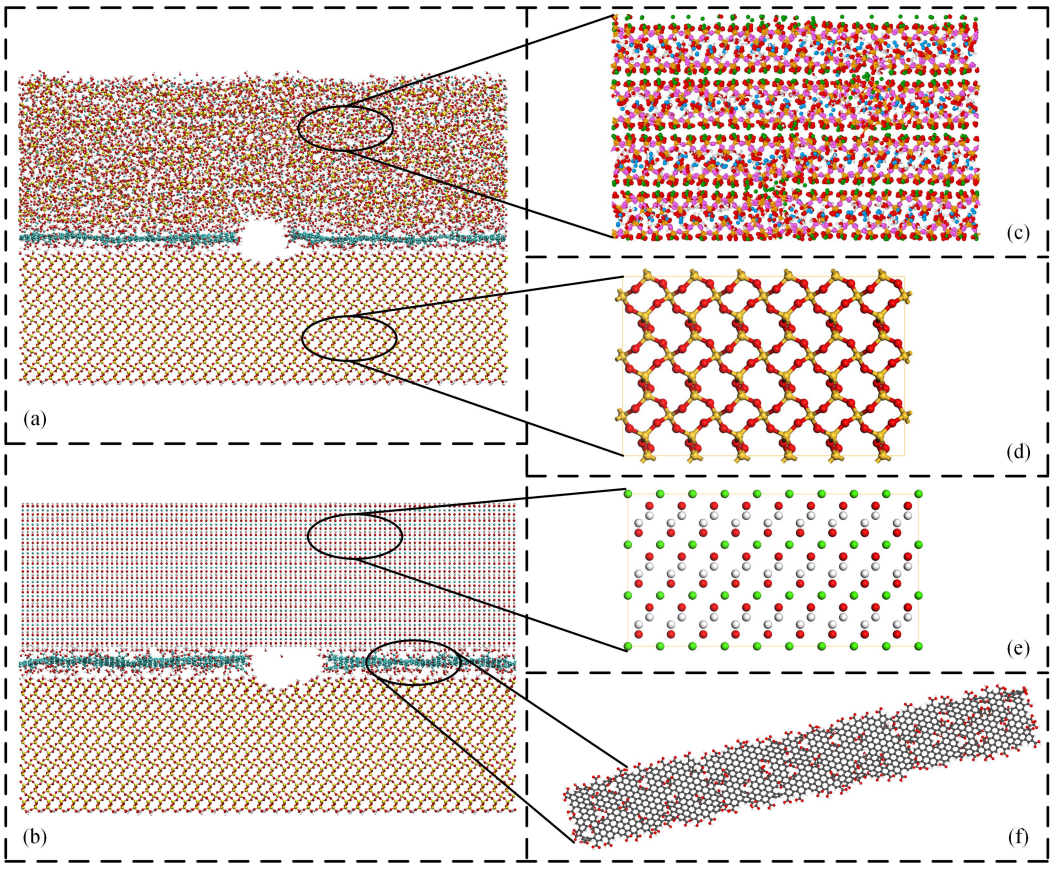

Figure 1: Construction of molecular models: (a) The interface between C-S-H and quartz. (b) The interface between CH and quartz. (c) C-S-H chains with C/S ratio of 1.7. (d) The unit cell of quartz. (e) CH unit cell. (f) GO sheet embedded in the interface. The green, blue, yellow, red, gray and white balls represent interlayer calcium, intralayer calcium, silicon, oxygen, carbon and hydrogen, respectively.

amorphous C-S-H structure, as shown in Fig. 1 (c). Please refer to our previous work [49] for more details about the minimizing, GCMC and reaction procedure. Crystals enriched in $Ca(OH)_2$ have also frequently been detected in the ITZ of cementitious composites in addition to C-S-H [50, 51, 52]. Therefore, both the C-S-H and CH components in the ITZ must be taken into account if we are to comprehend the mechanical characteristics of the ITZ. The C-S-H/quartz and CH/quartz structures are the two interfacial structures we generated after simplifying the aggregate portion to quartz crystals, as illustrated in Fig. 1 (a) and (b). Fig. 1 (e) is the crystal structure of CH [53], with unit cell

lattice parameters $a = b = 3.5862$ Å$, c = 4.8801$ Å, $\alpha = \beta = 90°$, $\gamma = 120°$. As shown in Fig. 1 (d), unit cell of α-quartz ($a = b = 4.913$ Å$, c = 5.4052$ Å, $\alpha = \beta = 90°$, $\gamma = 120°$) is used as the quartz phase. Graphene oxide (GO) sheets were embedded in the C-S-H or CH quartz interfaces to improve the fracture toughness of the fragile ITZ phase. Fig. 1 (f) shows the schematic model of GO atomic structure, expanded from the graphene unit cell with lattice parameters $a = 2.46$ Å$, b = 4.26$ Å$, c = 3.4$ Å and $\alpha = \beta = \gamma = 90°$. Since the oxygen atoms in -COOH functional groups are 20% of the number of carbon atoms in GO, corresponding carbon atoms should be removed in order to produce the desired number of -COOH groups. The functional groups were then randomly distributed at the edge and inside of graphene skeleton. Last, the optimized GO structures were inserted into the gap (10 Å) of the C-S-H/quartz and CH/quartz interfaces to enhance the mechanical properties of the interface phase.

2.1.2. Force field and loading process

In this research, the Large-scale Atomic/Molecular Massively Parallel Simulator (LAMMPS) [54] was used for all MD simulation operations. The amorphous C-S-H phase which is congruent with experimental evidence that results from the reaction of water molecules with Ca^{2+} ions or Silica tetrahedron is described, using the reactive force field (ReaxFF) [55]. Using the ReaxFF, water molecules will dissociate in the simulation to produce the Si-OH and Ca-OH groups. A general force field for clay phases (ClayFF) [56, 57] was employed to calculate the atomic interactions in C-S-H, CH and quartz crystal during the tensile procedure. ClayFF, a parameterized force field, is used to characterize systems with simple oxides, hydroxides, and oxyhydroxides. Only the bonds in hydroxyls are explained using the bond stretch and bond angle bend expressions; all metal-oxygen interactions are represented using Lennard-Jones and Coulomb potential. As a result, it works well with other complicated structures. For a variety of silica mineral systems, the usefulness of this force field in forecasting the structure and binding strength has been demonstrated [58, 59, 60]. The atomic potential in the GO phase was described using the consistent-valence force field (CVFF) [61], which has been demonstrated being effective for organic substances [62]. In this work, standard Lennard–Jones (12-6) potential terms between CVFF and ClayFF phases were mixed using geometric (Lorentz-Berthelot) combining rules [63].

Throughout all the MD tensile simulations, the interface models were subjected to uniaxial tensile displacement with a strain increment of 10^{-6} per femtosecond, and the time step was set to 0.1 femtoseconds. Before applying tensile loads, the entire interface system needs to be run for 1 nanosecond at 300 K and

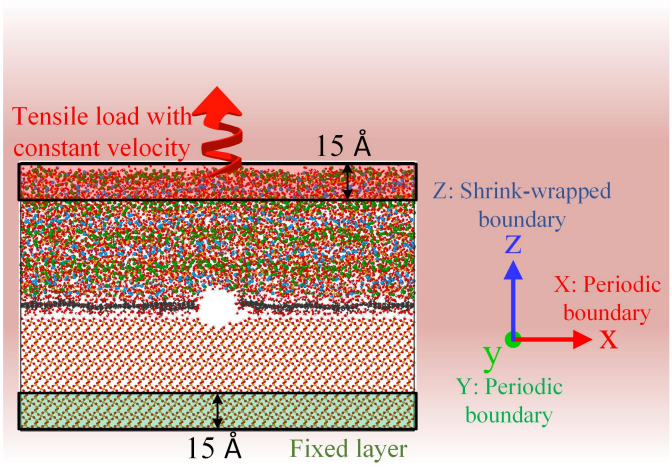

Figure 2: The loading and boundary conditions of MD system.

0 atm under an isothermal–isobaric ensemble (constant temperature and constant pressure ensemble, NPT), to establish a fully balanced interfacial structure. As the tensile process progressed with T = 300 K, the ensemble of interface system was then switched to a canonical ensemble (constant volume and constant temperature ensemble, NVT). As shown in Fig. 2, by setting the atom's velocity to zero, a layer of 15 Å was fixed at the bottom of quartz atoms. On the contrary, a layer of 15 Å on top of the C-S-H or CH phase were provided with a constant velocity in the z direction (perpendicular to the interface) as the tensile load. Periodic boundary conditions (PBC) were applied to X and Y axes. If the Z-axis direction is also set to PBC, the atoms at the top and bottom of the box will interact and form a new interface, which is not desired result. Therefore, we set the Z-axis direction to shrink-wrapped boundary condition, which allows the boundary of the simulation box to change synchronously with the maximum or minimum coordinates of the atoms and cuts off the interactions of the atoms across the box.

2.2. Finite element model

2.2.1. Model construction

At the macroscale, a model that incorporates the different phases of cement paste, aggregates, and ITZ, as well as the distribution of C-S-H and CH is need. Fig. 3 shows the distribution of diameters of aggregates in an ideal concrete model. The 2D Walraven-Fuller curve was chosen for the aggregates gradation

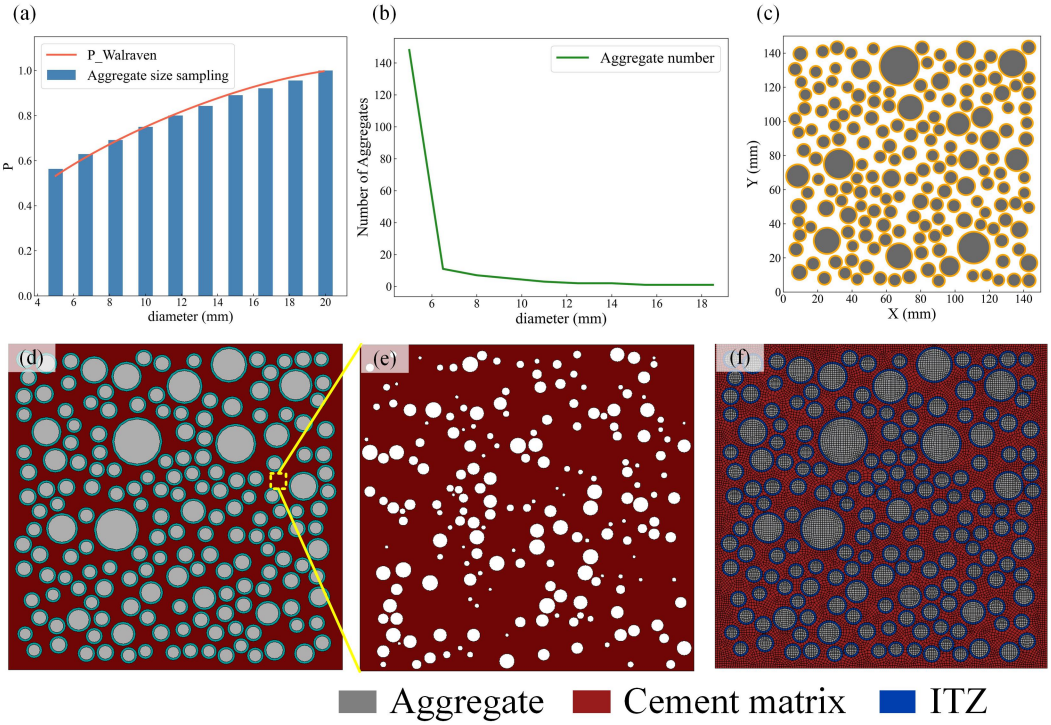

Figure 3: Distribution of the diameters of aggregates in concrete finite element model and 2D Finite element model of concrete with aggregates, cement paste and ITZ. (a) The 2D Walraven-Fuller curve of aggregates gradation. (b) Numbers of aggregates at different diameters. (c) Location and size of aggregates in a $150mm \times 150mm$ square concrete sample. The gray circles represent aggregates. (d) Finite element model of concrete sample, in which the annulus around the aggregates represent the ITZ. (e) Representative volume element (RVE) of cement matrix with pores. (f) Meshed concrete sample with different materials assigned. In (f), the gray, dark red and dark blue elements represent material of aggregates, cement matix and ITZ, respectively.

of the FEM model, as can be seen from Fig. 3 (a). Walraven-Fuller curve can be calculated from the following equation,

$$\begin{aligned} P_d =& 1.065 \times \left(\frac{d}{D_{max}}\right)^{0.5} - 0.053 \times \left(\frac{d}{D_{max}}\right)^{4.0} - 0.012 \times \left(\frac{d}{D_{max}}\right)^{6.0} \\ & - 0.0045 \times \left(\frac{d}{D_{max}}\right)^{8.0} - 0.0025 \times \left(\frac{d}{D_{max}}\right)^{10.0} \end{aligned} \tag{1}$$

where P_d is the percentage by weight of aggregates with diameter not greater

than d, and D_{max} is the diameter of the largest aggregate. Here, P_d is a cumulative value and the maximum value is $P_{D_{max}} = 1$.

The total volume fraction of aggregates to concrete was set to 40%. By sampling from this Walraven-Fuller curve, about 200 aggregates with diameters between 5 and 20mm was generated. Fig. 3 (b) presents the numbers of aggregates at different diameters. After obtaining diameter data of all the aggregates, we need to randomly disperse the aggregates in the concrete specimen model. A python script was used to automatically drop the aggregates. We partitioned the entire model into grids with a spacing of 0.2mm in order to speed up and improve the program's success rate when placing aggregates. When the being placed aggregate is detected as not satisfying the minimum distance from other aggregates, it will randomly move its center within the grid. It will be redelivered if the aggregate still not match the requirements after several attempts of movement. Fig. 3 (c) shows the location and size of all the aggregates in a $150mm \times 150mm$ square concrete sample. In Fig. 3 (d), the finite element model was established and was divided into three region: cement paste (dark red), ITZ (green annulus) and aggregates (gray). Calcium hydroxide and C-S-H are the two main hydrate phases that dominate the microstructural development of Portland cement, where C-S-H is mainly deposited close to the cement particles and CH is mainly deposited close to the pores. Here, we set the volume fractions of C-S-H, CH, and micropores in matrix to be 77%, 8%, and 15%, respectively. Similarly, the fraction of C-S-H, CH and pores in the ITZ phase were set to 57%, 13% and 30%, [52]. In Fig. 3 (e), a representative volume element (RVE) model of cement matrix only was constructed to investigate the overall damage evolution of cement paste. As shown in Fig. 3 (f), parameters of cement matrix, ITZ and aggregate calculateed from homogenization of C-S-H , CH, Quartz, C-S-H/GO(if any)/quartz and CH/GO(if any)/quartz were attributed to the corresponding region.

2.2.2. Constitutive response of elements

In this article, ABAQUS was employed to perform simulations of finite element models. Cohesive elements with zero thickness were embedded in the whole model in order to simulate the crack expansion along an arbitrary path in the specimen. To match the morphological structure distribution, the cohesive elements that are dispersed in different regions (ITZ, matrix, aggregate.) and materials (C-S-H, CH, etc.) were automatically detected and given the relevant mechanical properties. The constitutive response of the cohesive elements can be defined by the traction-separation relation, as shown in Fig. 4. The key parameters, stiffness K, peak traction stress σ^{max} and fracture energy G^C, can be obtained from

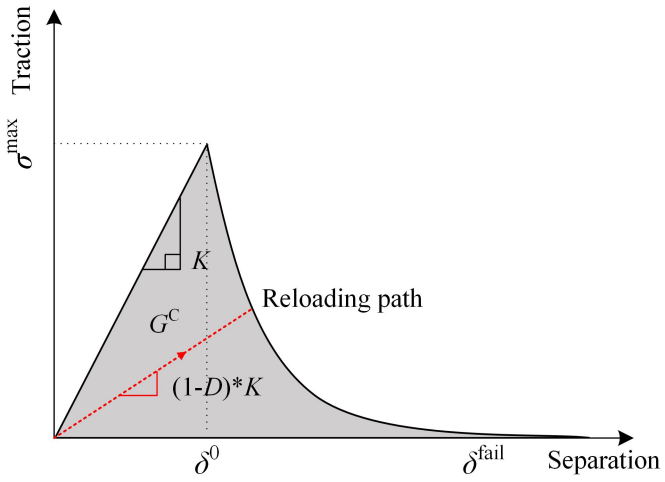

Figure 4: Traction-separation response of cohesive elements for damage evolution.

the molecular dynamics simulation results. The quadratic nominal stress criterion was used to determine whether the damage initiation of cohesive element. As shown in Eq. 2, when the sum on the left side of the equation equals to 1, the cohesive elements begin to suffer irreversible damage. Power law was used to define the fracture criterion of fracture energy. The evolution of the damage variable D is softened according to Eq. 3.

$$\left\{\frac{\langle\sigma_n\rangle}{\sigma_n^0}\right\}^2+\left\{\frac{\sigma_s}{\sigma_s^0}\right\}^2+\left\{\frac{\sigma_t}{\sigma_t^0}\right\}^2=1 \tag{2}$$

$$D=\int_{\delta_0}^{\delta^f}\frac{\sigma_{eff}d\delta}{G^C-G_0} \tag{3}$$

in which $\langle\rangle$ is the Macaulay bracket, $\sigma_n,\sigma_s,\sigma_t$ are the three components of traction stress vector. The corresponding peak value of traction at the initial damage are denoted by $\sigma_n^0,\sigma_s^0,\sigma_t^0$. G_0 is the elastic energy at damage initiation. σ_{eff} and δ are the effective traction and displacement.

In this paper, uniaxial tensile simulations are performed for single-aggregate and multi-aggregate FEM models, and the same boundary conditions are applied for both. As shown in the Fig. 5, the horizontal (U1) and vertical (U2) displacement of the bottom boundary of the model are constrained to be zero. The top boundary has only the horizontal displacement constrained to zero, and a displacement load was applied in the vertical direction to simulate uniaxial tension.

In order to get the magnitude of external force applied to the model, a reference point was created away from the top surface and the load was applied to the reference point. The force acting on the reference point during the simulation was equal to the magnitude of the applied external force.

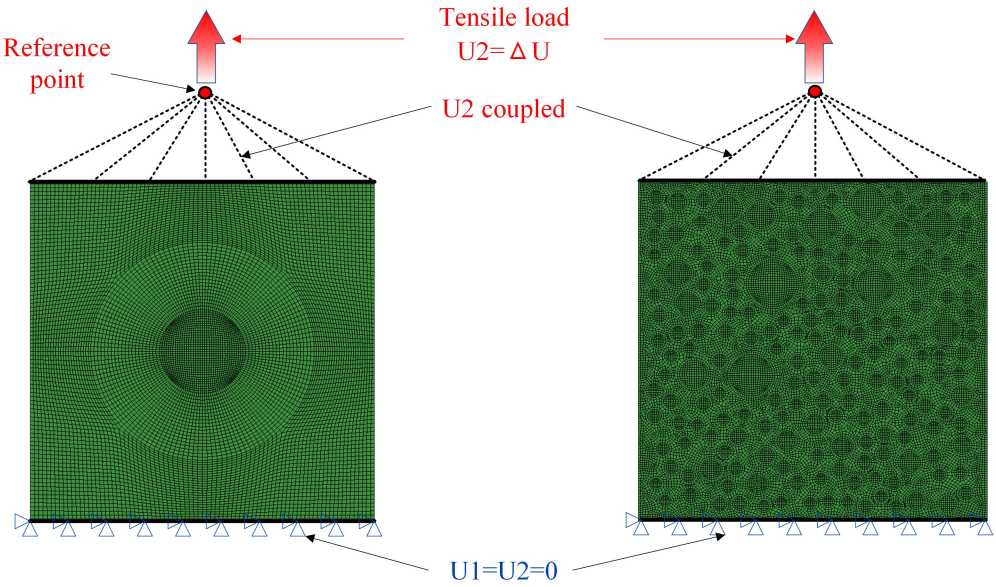

Figure 5: The loading and boundary conditions of single-aggregate and multi-aggregate FEM model.

3. Results and discussion

At the atomic level, a fracture happens when the bonds between atoms are broken along a fracture plane, generating new surfaces. The theoretical strength of the material is therefore determined by the interaction between atoms. To describe a material's capacity to resist crack growth, the energy release rate (G) and stress intensity factor (K) are typically used parameters,

$$W = \frac{1}{2}\int_0^a p(x,0)\bar{u}T\,dx \tag{4}$$

in which the W is the work done to extend the crack, the $p(x,0)$ is the crack normal stress distribution in the corresponding crack-free body. $\bar{u}$ is the total opening displacement of crack at position x and T represents the thickness of the

body. The energy release rate of the crack propagation can be expressed by the following equation,

$$G = \frac{dW}{dA} = \frac{1}{2}\int_0^a p(x,0)\frac{d\bar{u}}{dA}T\,dx \tag{5}$$

where A is the area of the corresponding crack. Fig. 6 demonstrates how to determine the crack area for a given frame from the results of the MD simulation. The blue translucent bubble in Fig. 6 (a) represents the pores of crack during tension. The free volume of pores is determined by calculating real space function in the MD simulation box. It was performed by a Multifunctional Wavefunction Analyzer (Multiwfn) [64] using 1.8 times van der Waals radius as the full width at half maximum of Gaussian function. As shown in Fig. 6 (b), the crack area is determined by the projection of the free volume on the horizontal plane.

The energy release rate and the stress intensity factor are two parameters frequently used to describe the fracture characteristics of materials. For the opening mode (Mode-I), the relationship between critical energy release rate G_C and fracture toughness K_{IC} can be expressed by Eq. 6,

$$G_C = \frac{K_{IC}^2}{E'},\ E' = \begin{cases} E & ,plane\ stress \\ \frac{E}{1-\upsilon^2} & ,plane\ strain \end{cases} \tag{6}$$

where E' is related to Young's modulus E and Poisson's ratio υ. Here the plane strain case is applicable to our current study.

3.1. Fracture properties of matrix and aggregate phase at nanoscale

In order to monitor the crack area, we need to create an initial crack in the atomic structure and make it the location where the crack starts. The atoms in the structure will be removed when the coordinates fall within an ellipse whose diameter of the major axis is five times the minor axis, as shown in Fig. 7 (a). To keep the system electrically neutral, the selected atoms will be deleted in the form of a group of atoms with a total charge of zero. The values of critical energy release rate are plotted against the size of initial crack in Fig. 7 (b). The size of the initial crack can affect the plastic deformation region in the structure, and to exclude this effect, structures with two different C/S ratios were used to calculate the energy release rates at different initial crack sizes. Compared with $G_C = 1.72 \pm 0.29 J/m^2$ of $C/S = 1.65$ in the literature [65] and $G_C = 2.0 J/m^2$ of $C/S = 1.0$ in [66], the critical energy release rate of two C-S-H structure with $C/S = 1.7$ and $C/S = 1.0$ are $G_C = 1.81 \pm 0.13 J/m^2$ and $G_C = 2.89 \pm 0.31 J/m^2$, respectively. The value of

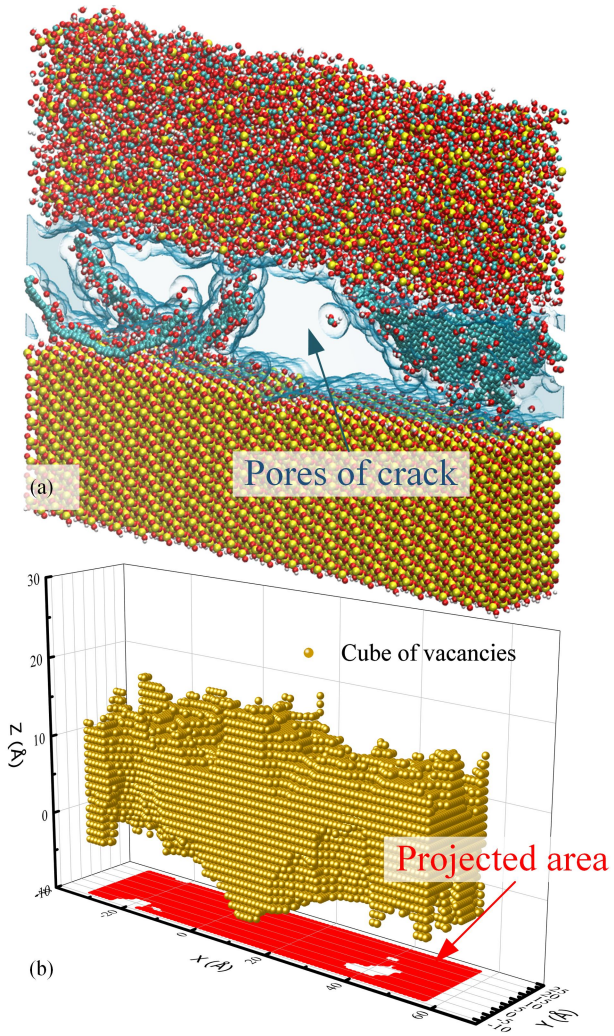

Figure 6: Estimation of the crack area in a MD simulation. (a) Schematic diagram of the pores created by the crack. (b) Spatial distribution of the cubes of the crack pores, and its projection on the horizontal plane.

the energy release rate barely changes after the length of initial crack is larger than 20Å. In the subsequent MD simulations, initial crack length of 30Å was adopted for all phases and structures.

Fig. 8 (a) and (b) shows the atomic snapshots of quartz, CH, and C-S-H at strain = 0.1 and 0.2. The volumes of simulation boxes for quartz, CH and C-S-H are 178.50Å $\times$ 31.11Å $\times$ 98.13Å, 178.71Å $\times$ 31.52Å $\times$ 86.48Å and 178.68Å $\times$

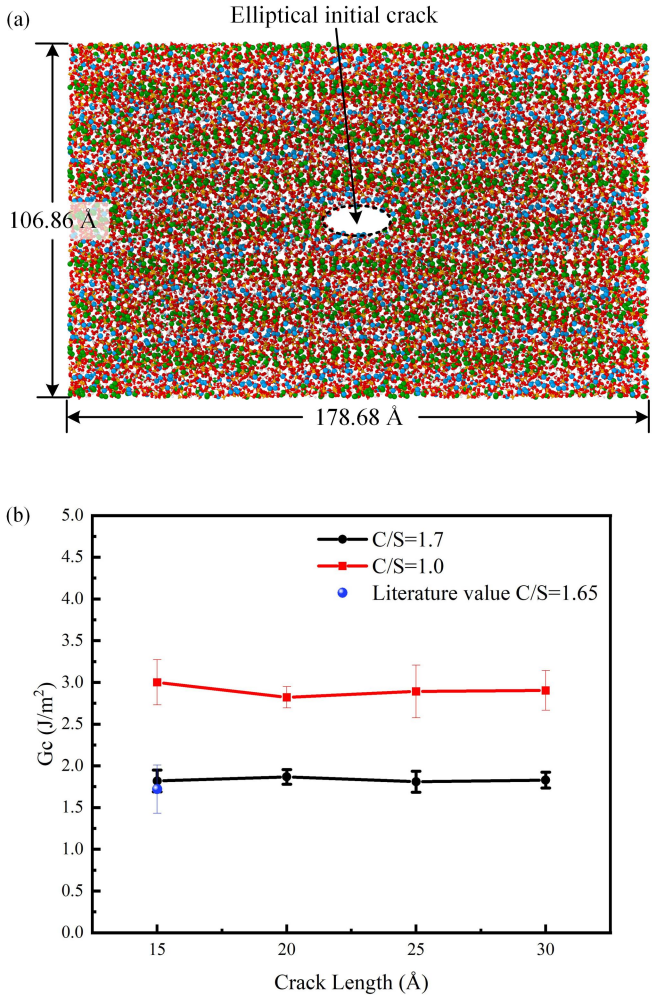

Figure 7: Effect of initial crack size on MD simulation results. (a) Illustration of the elliptical initial crack in the MD model, taking C-S-H as an example. (b) The critical energy release rate of C-S-H at different initial crack lengths.

31.42Å $\times$ 106.86Å, respectively. The stress-strain curves of C-S-H, quartz and CH phases under uniaxial stretching are shown in Fig. 8 (c). The stress of quartz reaches a peak value of 42 GPa when the strain approaches 0.1, and then the crack starts to expand drastically, accompanied by a sharp drop in stress and brittle damage. Due to the effect of the initial crack, a significant number of dislocations are formed in the vicinity of the crack before the material is damaged, so the stress-strain curve before the stress peak is not very typical linear. At high

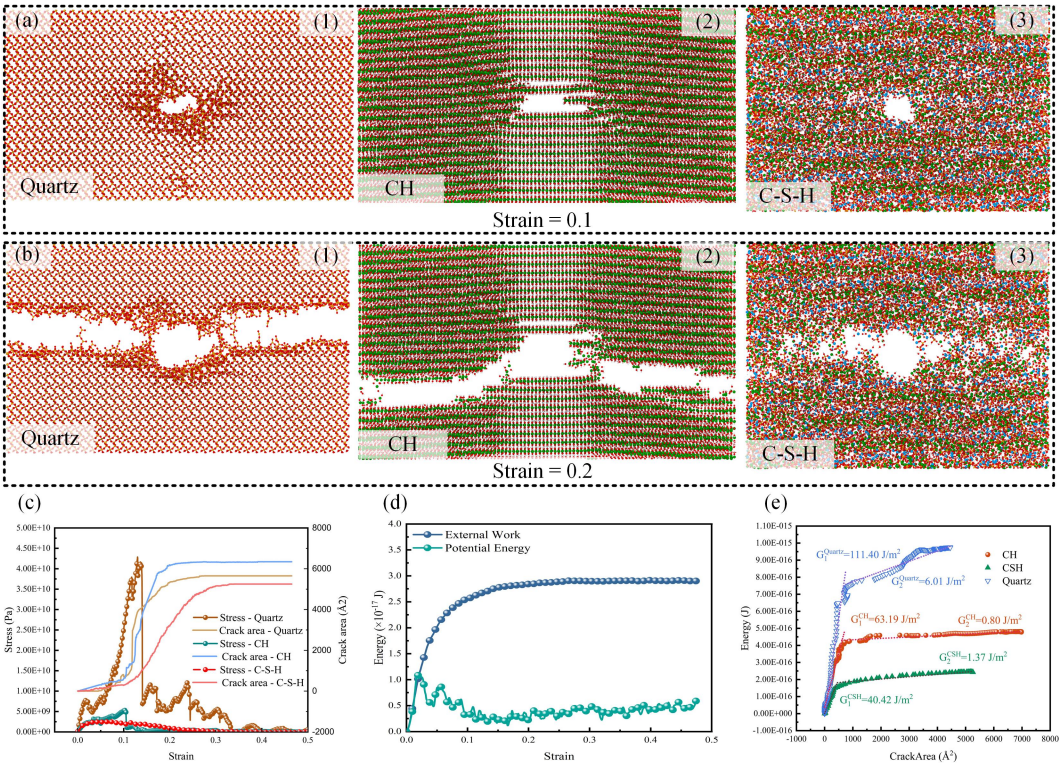

Figure 8: Atomic snapshot of quartz, CH, and C-S-H at (a) strain = 0.1 and (b) strain = 0.2. (c) Stress and crack area curves with strain. (d) Energy-strain curves. (e) Energy-crack area curve of quartz, CH and C-S-H phases.

strain, the crack quickly spreads horizontally (in the direction of the long axis of the initial crack) and penetrates through the whole cross-section of simulation box where the interatomic interaction near the crack are insufficient to sustain the stresses produced by tensile deformation. Similar to quartz, CH also exhibits apparent brittle fracture after reaching a peak tensile strength of 4.7 GPa close to a strain of 0.9. The cracks in CH grow at an angle inclined downward near the initial crack, while in most of the other regions grow along the horizontal direction (along the interlayer of Ca-OH atoms). Unlike the quartz and CH phases, C-S-H phase has more noticeable ductile damage behavior at nanoscale. The stress reaches a peak of 2.5 GPa at a strain of 0.06 and steadily declines to zero as the strain climbs to 0.3. Furthermore, the crack area versus strain curves shows that the crack extension rate of C-S-H is about twice lower than that of quartz and CH. Even at high strains, there are still some adherent atoms (mainly some short

silicate tetrahedron chains) playing a positive role in the connection of the crack, which contributes to the blunting of the crack tip and is one of the main factors of the C-S-H ductile response. The energy variation curve of the C-S-H phase during tensile process is depicted in Fig. 8 (d). Almost all of the external work on the system is stored as elastic mechanical potential energy during the elastic deformation stage ($strain < 0.02$), during which the crack does not propagate. Plastic deformation occurs in the system and the crack area begins to expand as the strain keeps increasing, it causes that the external work is used to generate a new surface or is dissipated by plastic deformation [67]. Fig. 8 (e) shows the work done by the average stress at both sides of the crack area in the quartz, CH and C-S-H systems. The energy increases very fast at the start of the crack expansion because the stress still maintains a high value despite its rapidly reducing. After the crack starts to expand smoothly, the energy increases slowly and steadily. By tracing the cracks, we were able to determine the fracture toughness and critical energy release rate of quartz, CH, and C-S-H phases (shown in Table 1), which are important parameters that determines the fracture response of the aggregate and cement matrix phase in the macroscale model. And we also obtained Young's modulus (E), shear modulus (G), bulk modulus (K), and Poisson's ratio (ν) in order to describe the elastic response of different phases' materials.

After performing deformations on the MD model, the elastic stiffness coefficients C_{ijkl} can be calculated from the components of the stress and strain tensors.

$$C_{ijkl} = \frac{\partial \sigma_{ij}}{\partial \varepsilon_{ij}}\bigg|_{T,\varepsilon_{kl}} = \frac{1}{V_0}\frac{\partial^2 A}{\partial \varepsilon_{kl}}\bigg|_{T,\varepsilon_{ij},\varepsilon_{kl}} \tag{7}$$

where V_0 is the initial volume (undeformed) of the computed system, A is the Helmholtz free energy, σ and ε are the stress and strain components. Then bulk and shear modulus are obtained using Voigt–Reuss–Hill (VRH) approximation [68].

$$G_V = \frac{1}{15}\left[C_{11}+C_{22}+C_{33}+3\left(C_{44}+C_{55}+C_{66}\right)-\left(C_{12}+C_{13}+C_{23}\right)\right] \tag{8}$$

$$G_R = 15\left[4\left(S_{11}+S_{22}+S_{33}-S_{12}-S_{13}-S_{23}\right)+3\left(S_{44}+S_{55}+S_{66}\right)\right]^{-1} \tag{9}$$

$$K_V = \frac{1}{9}\left[C_{11}+C_{33}+2\left(C_{12}+C_{13}+C_{23}\right)\right] \tag{10}$$

$$K_R = [S_{11} + S_{22} + S_{33} + 2(S_{12} + S_{13} + S_{23})]^{-1} \tag{11}$$

$$K_{VRH} = \frac{K_V + K_R}{2} \tag{12}$$

$$G_{VRH} = \frac{G_V + G_R}{2} \tag{13}$$

Finally, we can get the average Young's modulus (E) and the Poisson's ratio (ν) by Eq. 14, 15:

$$E = \frac{9G_{VRH}}{3 + G_{VRH}/K_{VRH}} \tag{14}$$

$$\nu = \frac{3 - 2G_{VRH}/K_{VRH}}{6 + 2G_{VRH}/K_{VRH}} \tag{15}$$

Table 1: Fracture and elastic properties of different phases in matrix, ITZ and aggregates.

Phase	$\mathbf{G_C(J/m^2)}$	$\mathbf{K_{IC}(MPa \cdot m^{\frac{1}{2}})}$	**K (GPa)**	**G (GPa)**	**E (GPa)**	ν
C-S-H	1.81	0.349	44.10	17.82	47.10	0.32
CH	3.43	0.428	42.46	18.40	48.22	0.31
Quartz	8.60	0.904	38.97	42.85	94.06	0.10
C-S-H/Quartz	0.18	0.093	38.98	16.95	44.42	0.31
C-S-H/GO/Quartz	0.27	0.147	67.67	26.54	70.42	0.33
CH/Quartz	0.22	0.125	41.44	17.04	44.97	0.32
CH/GO/Quartz	0.38	0.173	63.88	27.27	71.62	0.31

3.2. Fracture properties of ITZ phase at nanoscale

After the simulation of the three representative phases in the cement matrix and aggregate, our attention turns to the structure in the ITZ as this area is more prone to failure and generally experiences cracks first compared to the matrix. To replicate the fragile interfacial connection between cement matrix and aggregate in ITZ, C-S-H and CH were individually in touch with quartz in the z-direction to create an interfacial region with a thickness of around 10Å. Grand Canonical Monte Carlo simulation was carried to introduce water molecules into the interfacial region. As an control, GO sheets were inserted into the interfacial system

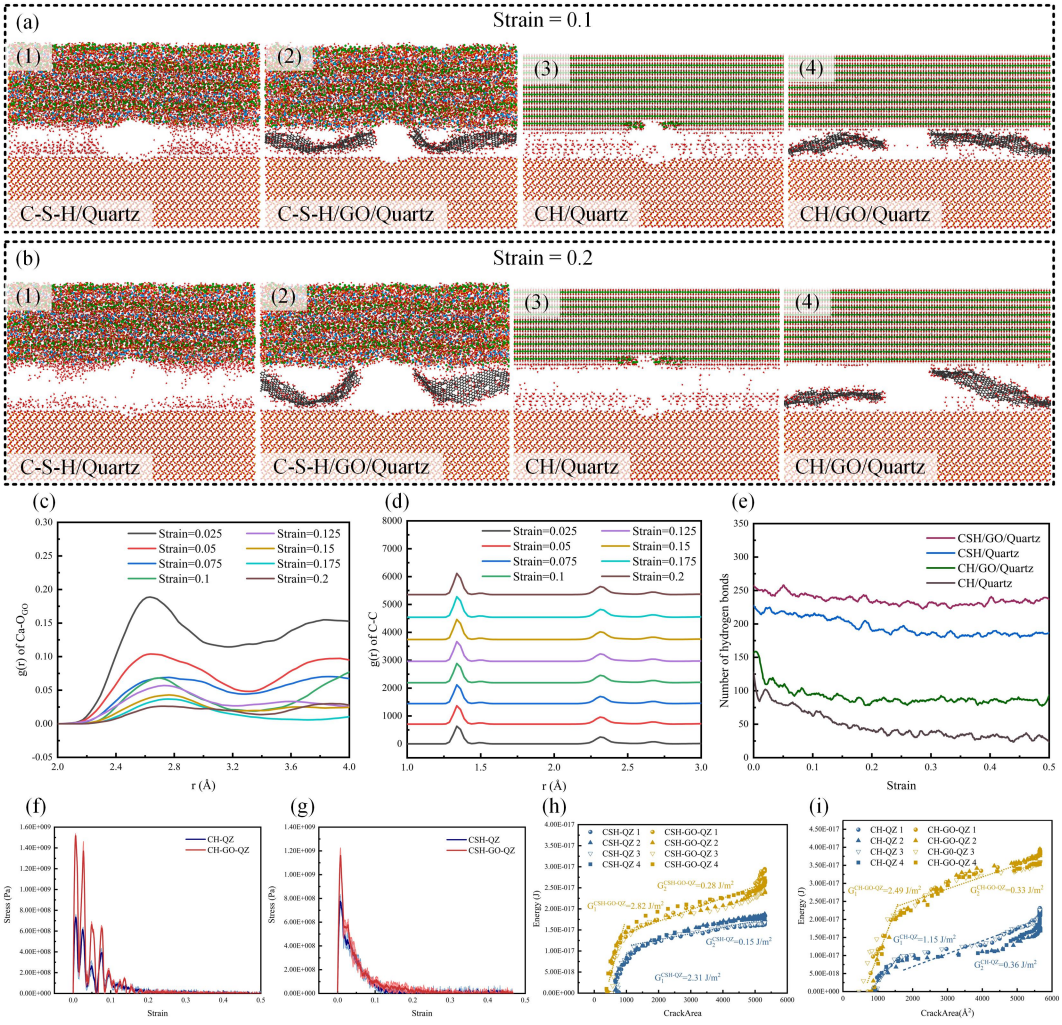

Figure 9: Simulation results of the interface between quartz and C-S-H, CH. Atomic snapshot of C-S-H/(GO)/quartz and CH/(GO)/quartz interfaces at (a) strain = 0.1 and (b) strain = 0.2. (c) Radial distribution function (RDF) of calcium atoms in the C-S-H phase and oxygen atoms in the GO sheet. (d) RDF of carbon atoms in the GO sheet. (e) The number of hydrogen bonds in the contacting interface during tensile deformation. Stress-strain curve of (f) CH/(GO)/quartz interfaces and (g) C-S-H/(GO)/quartz interfaces. Energy-crack area curve of (h) C-S-H/(GO)/quartz interfaces and (i) CH/(GO)/quartz interfaces.

(correspondingly reducing the number of water molecules) to simulate the effect of nano-fillers on ITZ enhancement and toughening.

The atomic snapshots for the four interfacial systems C-S-H/(GO)/quartz and

CH/(GO)/quartz at strains of 0.1 and 0.2 are shown in Fig. 9 (a) and (b).The yield strain of both C-S-H/quartz and CH/quartz decreases to roughly 0.007 under the impact of the poor interfacial bonding, which is in distinct contrast to 0.06 for the pure C-S-H phase and 0.1 for the CH phase. However, the addition of GO in the interfacial region plays a significant role in enhancing their ductility: the yield strain of C-S-H/GO/quartz and CH/GO/quartz increases to about 0.01 (see the stress-strain curve in Fig. 9 (f) and (g)). The improvement on the strength of adding GO in the interfacial system is more obvious, the yield strengths of C-S-H/(GO)/quartz and CH/(GO)/quartz system increases by 49.61%and 106.54%, respectively. This enhancement effect can be explained by the results of the RDF and hydrogen bond analysis [20]. Fig. 9 (c) illustrates the RDF of the Ca-O atom pair, where Ca is the intralayer and interlayer calcium atoms in C-S-H and O is the oxygen atoms in the carboxyl functional groups on the GO sheet. At a low strain of 0.025, the first peak of the Ca-O_{GO} pair appears near 2.63Å. As the strain increases, the peaks are gradually shifted to near 2.79Å (strain = 0.175) and finally there is almost no obvious peak value (strain of 0.2). At the same time, the peak also becomes to have a broader distribution with the increase of strain. This indicates that the originally stable Ca-O_{GO} connection in the interface is gradually elongated by the tensile deformation until finally there is no significant spatial correlation between Ca-O_{GO} pair [69]. The interactions between other atoms do not respond to strain in a way that the Ca-O pair does. This implies that the connection between calcium and oxygen in the interfacial system plays the most dominant role in resisting deformation and crack. For instance, the RDF curve for the C-C pair (Fig. 9 (d)) shows no sensitive changes to strain, with only a small increase of the peak value caused by the bending of the GO sheet during deformation.

The hydrogen bonds in the interface region, in addition to the atomic interactions between Ca and O_{GO}, also play a important role in the resistance to tension. Fig. 9 (e) shows the curves of the number of hydrogen bonds with strain in the four interfacial systems. In the C-S-H/(GO)/quartz system, there are 64.74% $\sim$ 77.34% more hydrogen bonds than in the CH/(GO)/quartz system. This difference can be attributed to the C-S-H phase's rougher surface and a large number of free hydroxyl groups, which enable the C-S-H phase to form more hydrogen bonds with GO. The addition of GO to the interface considerably increases the number of hydrogen bonds even though the amount of oxygen atoms in GO is much less than the oxygen atoms of water molecules in the interface without GO. Finally, The critical energy release rate and fracture toughness for the four interfacial systems were determined, as in the previous section, by tracking the energy

versus crack area of the system. These results, together with other elastic property parameters, are reported in Table 1. Fig. 10 (a) shows the fracture toughness of C-S-H/CH/(GO)/quartz composites phases. Compared to the results of Bauchy et al. [66] and Zhang et al. [65], the fracture toughness of C-S-H with a C/S of 1.7 in this paper is slightly lower than that of the reference sample with a C/S ratio of 1.65. This is mainly due to the fact that the increase in the C/S ratio leads to more defects in the silicate tetrahedron chains, and the decrease in the average chain length leads to a corresponding decrease in the fracture properties of C-S-H [70, 71]. The addition of GO increased the fracture toughness of the C-S-H/quartz and CH/quartz systems by 58.06% and 38.40%, respectively. The MD approach used to calculate the fracture parameters in this paper is applicable to other similar cementitious composite systems. As shown in Fig. 10 (b), nanoscale simulations can also be used to examine the polymer-reinforced concrete system represented by the C-S-H/resin interface and investigate how the material design approaches affect the system's fracture response.

3.3. Fracture simulation at macroscale

Due to the limitations of computational resources, many reported studies ignore the effect of ITZ in macroscopic models or simply set the mechanical properties of ITZ as a linear reduction of the cement matrix [72, 73, 74]. Pores in the cement matrix and ITZ must be taken into account in order to upscale the mechanical properties of the individual phases from microscopic to macroscopic. The different phases that correspond to the MD simulations will therefore be treated as porous materials and homogenized using Eq. 16, 17, 18, 19given by the Mori-Tanaka method [75].

$$K_{hom} = \frac{\sum_i V_i K_i \left(1 + A_r \left(\frac{K_i}{K_r} - 1\right)\right)^{-1}}{\sum_i V_i \left(1 + A_r \left(\frac{K_i}{K_r} - 1\right)\right)^{-1}} \tag{16}$$

$$G_{hom} = \frac{\sum_i V_i G_i \left(1 + B_r \left(\frac{G_i}{G_r} - 1\right)\right)^{-1}}{\sum_i V_i \left(1 + B_r \left(\frac{G_i}{G_r} - 1\right)\right)^{-1}} \tag{17}$$

$$A_r = \frac{3K_r}{3K_r + 4G_r} \tag{18}$$

$$B_r = \frac{6K_r + 12G_r}{15K_r + 20G_r} \tag{19}$$

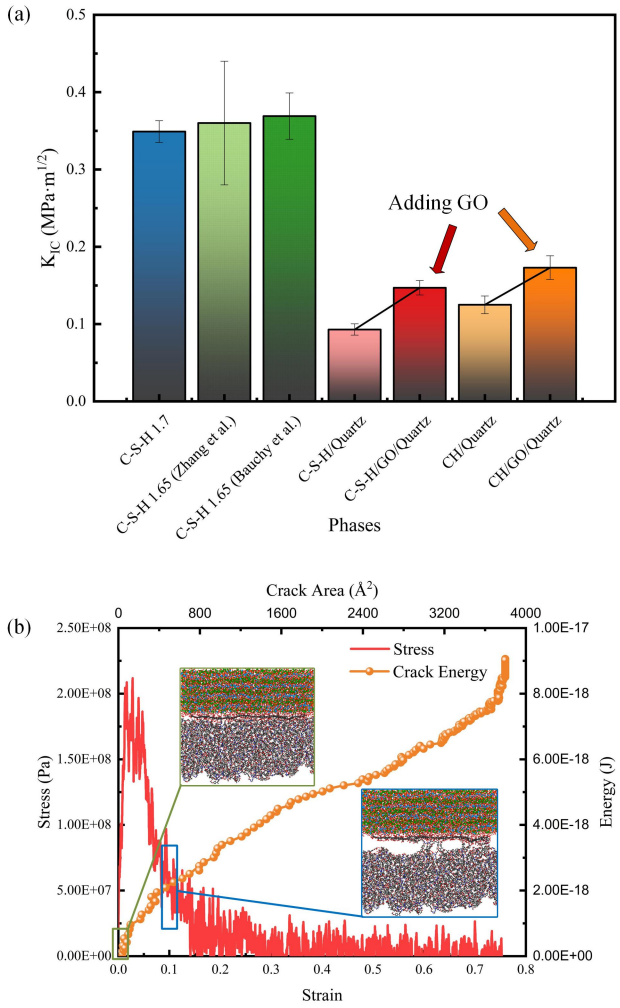

Figure 10: Fracture toughness of different phases (a) and extended application of the fracture properties tracking method in this article to the resin/cement composites system (b).

The volume fraction of cement paste components can be written as a function of w/c according to the empirical equations [76]:

$$f_{clin}(\xi) = \frac{1-\xi}{1+\frac{\rho_{clin}}{\rho_{H_2O}}(w/c)} \tag{20}$$

$$f_{H_2O}(\xi) = \frac{\rho_{clin}(w/c - 0.42\xi)}{\rho_{H_2O}\left[1 + \frac{\rho_{clin}}{\rho_{H_2O}}(w/c)\right]} \tag{21}$$

$$f_{hyd}(\xi) = \frac{1.42\rho_{clin}\xi}{\rho_{hyd}\left[1 + \frac{\rho_{clin}}{\rho_{H_2O}}(w/c)\right]} \tag{22}$$

where f_{clin}, f_{H_2O}, f_{hyd} are the volume fractions of clinker, water, and hydration products, respectively. ξ $(0 \leq \xi \leq 1)$ is the degree of hydration. Fig. 11 shows a schematic diagram of the RVE for cement paste only in several different hydration states. In order to facilitate the subsequent calculation and unified discussion, here we take RVE for the fully hydrated cement paste with w/c=0.42 for finite element simulation calculation.

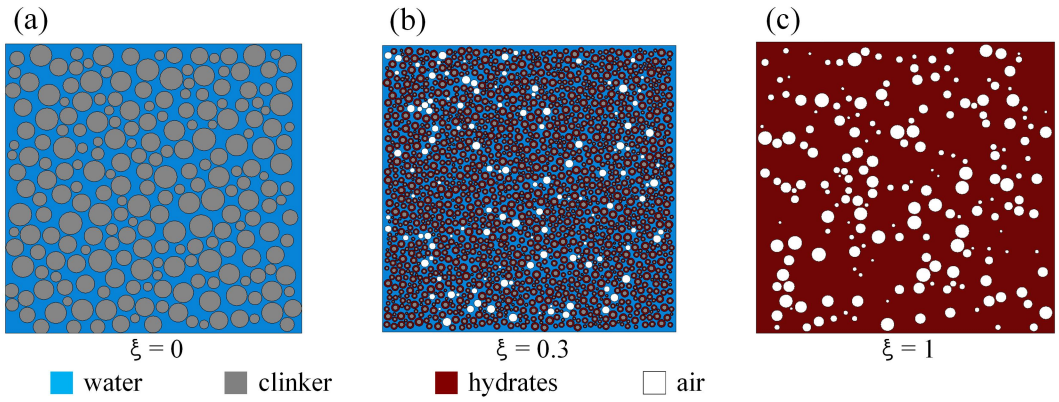

Figure 11: Changes in the composition of cement paste at different degree of hydration.

Table 2: Volume ratio and porosity of different components in RVE of matrix.

Level	**Phase**	**Density** (g/cm^3)	**Porosity**	**Volume**
C-S-H solid	Globules	2.39	0.18	-
C-S-H gel	LD-C-S-H	1.93	0.52	0.67
	HD-C-S-H	2.13	0.237	0.25
CH	CH	2.24	0.28	0.08

Fig. 12 (a) shows a FEM model of cement paste only. As mentioned above, at hydration state $\xi = 1$ and w/c=0.42, we can assume that clinker in cement paste

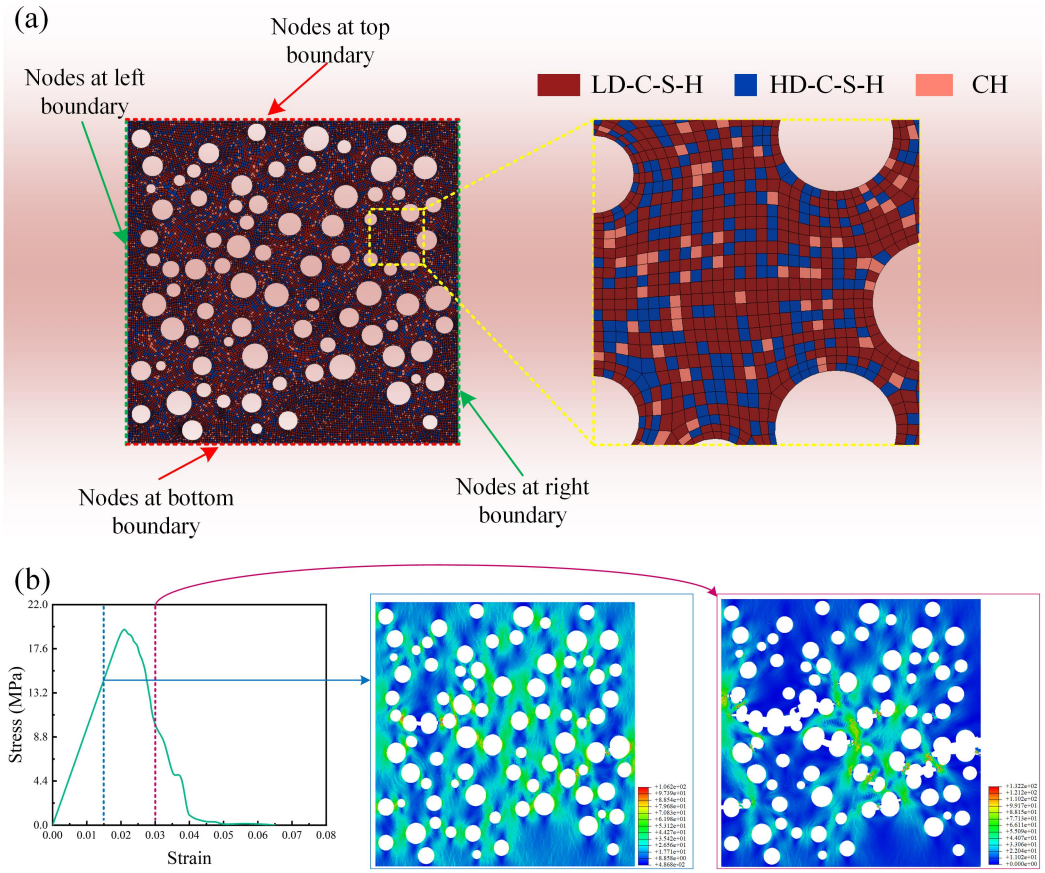

Figure 12: (a) FEM model of cement paste RVE and composition distribution. (b) Stress-strain curve of RVE and stress distribution at strain = 0.015, and 0.03.

Table 3: Elastic and cohesive parameters of different phases in cement matrix for ABAQUS.

Materials	E **(GPa)**	G_{12} **(GPa)**	**v**	**Fracture Energy** G_n^C **(N/mm)**	σ_n^0 **(MPa)**	σ_{st}^0 **(MPa)**
LD-C-S-H	13.55	27.10	0.27	5.54	35.46	70.91
HD-C-S-H	19.37	38.75	0.28	7.92	50.69	101.37
CH	19.07	38.14	0.27	12.15	88.21	176.42

reacts completely with water, leaving only C-S-H, CH and porosity. According to the volume fraction and porosity of each phase such as high density (HD) and low

density (LD) C-S-H in references [72] (see Table. 2), based on the Mori-Tanaka scheme and micromechanics theory we get the results of parameters after the first step of the homogenization [77, 76, 78], as shown in Table. 3. Scale bridging simulations using continuum theories usually need selecting a sub-volume of RVE from a large bulk material and applying periodic boundary conditions to simulate the overall elasticity and damage evolution of the bulk material [79, 80, 81, 82]. Here, we build the PBC for cement paste RVE model by applying the constraint equation as follows.

$$u_x^{Left} - u_x^{Right} = 0 \tag{23}$$

$$u_y^{Top} - u_y^{Bottom} = \Delta u \tag{24}$$

Eq. 23 and 24 can be implemented by applying constraints to the nodes on the four edges of the model, as Eq. 25:

$$A_1 u_i^P + A_2 u_j^Q + ... + A_N u_k^R = \hat{u} \tag{25}$$

where N is the number of nodes on an edge, A_N is a constant coefficient of nodes' relative motion. i, j, k represent degree of freedom and $\hat{u}$ is the displacement of a dummy node, on which we can apply load on it.

Stress-strain curve of RVE is shown in Fig. 12 (b). The tensile stress in the RVE reaches a peak of 19.46 MPa at strain=0.02, however some of the elements have broken down and formed cracks which bridging two adjacent pores before the strain reaches 0.015. As the strain continues to increase, the number of cracks linking multiple pores gradually increases and tends to form penetration cracks through the entire model section. Finally, it breaks completely at strain=0.065 and the stress is reduced to zero. Since there are rare direct uniaxial tensile experiments on micro-scale cements, we refer to indirect tensile strength values obtained from flexural strength test and split tensile strength test in previous studies. Generally these indirect tensile strength values are not equal to the direct uniaxial tensile strength values, and split tensile tests tend to underestimate the actual strength values [83]. Moreover, the size of the specimen has a very strong influence on the tested strength values, the strength measured at the micro-scale can even be an order of magnitude higher than that tested on macro specimen [19]. Most of the split tensile strengths of cement paste reported in the literature are in the range of 3.56 MPa - 6.90 MPa [84, 85, 86, 87, 88], and most of the flexural strengths are in the range of 9.35 - 14.15 MPa [84, 19, 89, 90].

Even considering the underestimation of the experimental values, the tensile strength value of cement paste obtained from the simulations in this paper are still large. The overestimation of the tensile strength values in this paper is mainly affected by the following factors: 1. In order to simplify the modeling, the tendency of the distribution of C-S-H, CH and pores is not taken into account. C-S-H tends to be more concentrated in the periphery of the cement particles, and CH is more likely to be generated in the vicinity of pores and have preferential orientations. This morphological feature leads to inhomogeneous distribution of the strength and stiffness. In this study we randomly and uniformly distribute LD-C-S-H, HD-C-S-H, CH with pores, this idealized model is significantly different from the real cement paste morphology. 2. The finite element models in this paper was assumed that the specimens have w/c = 0.42 and are fully hydrated. Specimens cured for 28 d or earlier are often used for experimental tests, which have the strength values at least 30% lower than those of fully hydrated specimens [88]. The focus of this paper is on how to predict the effect of adding nano-additives on the tensile fracture properties of cementitious composites, and a side-by-side comparison of the predictive models considering with or without nano-additives, and the addition of different types of nano-additives, may be more meaningful for this multiscale model. This in turn guides researchers to design composites with better performance of toughness and crack resistance.

Table. 4 shows the volume ratios occupied by pores and four phases that correspond to the MD simulation in the cement matrix or ITZ. On the other side, the aggregates are envisioned as dense, voidless structure. There are higher porosity and more CH products in the ITZ compared to the matrix, which is consistent with the reported experimental results [77, 52]. For example, the CH to C-S-H ratio in the cement matrix is 8:77. The elements in the matrix region of the FEM model are randomly assigned the material properties of CH or C-S-H according to that ratio after homogenization of CH and C-S-H with a 15% porosity.

Table 4: Volume ratio of different components in cement matrix and ITZ.

Components	**matrix**	**ITZ**
Pores	15%	30%
CH	8%	-
C-S-H	77%	-
CH/(GO)/quartz	-	13%
C-S-H/(GO)/quartz	-	57%

Similar to the homogenization of the different components in cement ma-

trix, we also calculated the parameters of the main components of ITZ, C-S-H/(GO)/Quartz and CH/(GO)/Quartz, as listed in Table. 5. Then the second step of multi-phase homogenization was carried out to get the parameters of overall properties for cement matrix, ITZ, and aggregate. These three materials were used in the single-aggregate and multi-aggregate FEM model, which will be discussed in the following paragraphs. Two types of elements were used in ABAQUS: 4-node bilinear element for elastic materials, and two-dimensional cohesive element with four nodes for materials with damage of traction-separation law. The parameters applied for all different phases in the cohesive elements were listed in Table. 6. The Young's modulus (E) and Poisson's ratio (ν) of elastic materials were set to the same values as in the cohesive elements. Since the bond strength between the C-S-H layers is much smaller than the bond parallel to the direction of the SiO_4 tetrahedral chains, in this paper we considered the tensile properties when the loading direction is perpendicular to the C-S-H layers, to take the most fragile case in matrix and ITZ into account. However, the orientation of the C-S-H layer in actual cementitious materials is of random nature and will not be always perpendicular to the loading direction. Furthermore, too small shear strength will lead to larger distortion of the FEM model cells under uniaxial tensile loading, which is more difficult to converge. We set the shear modulus and strength to be twice that of normal direction, and such an approximate treatment will greatly reduce the difficulty of model convergence.

Table 5: Elastic and cohesive parameters of different phases in ITZ for ABAQUS.

Materials	E **(GPa)**	G_{12} **(GPa)**	**v**	**Fracture Energy** G_n^C **(N/mm)**	σ_n^0 **(MPa)**	σ_{st}^0 **(MPa)**
C-S-H/Quartz	7.73	15.47	0.25	0.22	5.20	10.39
C-S-H/GO/Quartz	12.27	24.55	0.26	0.41	9.22	18.43
CH/Quartz	7.83	15.67	0.26	0.26	5.81	11.63
CH/GO/Quartz	12.47	24.95	0.26	0.43	12.01	24.03

The single-aggregate model's stress distribution contours at three deformation (strain = 0.05, 0.1, and 0.15) is shown in Fig. 13. The stress distribution (max principal Stress) and damage state (damage variable D) for the models with and without GO modified ITZ are displayed in order to illustrate the features of local cracks. It can be seen that no cracks appear in both the pure sample and the GO-modified ITZ sample at low strains (damage variable in the legend is zero at $strain = 0.05$). There is a distinct stress concentration zone, that tends to extend

Table 6: Elastic and cohesive parameters of single/multi-aggregate models for ABAQUS.

Materials	E **(GPa)**	G_{12} **(GPa)**	**v**	**Fracture Energy** G_n^C **(N/mm)**	σ_n^0 **(MPa)**	σ_{st}^0 **(MPa)**
Cement	9.69	19.38	0.25	3.15	20.13	10.39
ITZ without GO	4.17	8.33	0.24	0.30	6.67	18.43
ITZ with GO	6.62	13.23	0.24	0.61	13.89	11.63
Aggregate	31.65	63.30	0.14	51.43	123.43	24.03

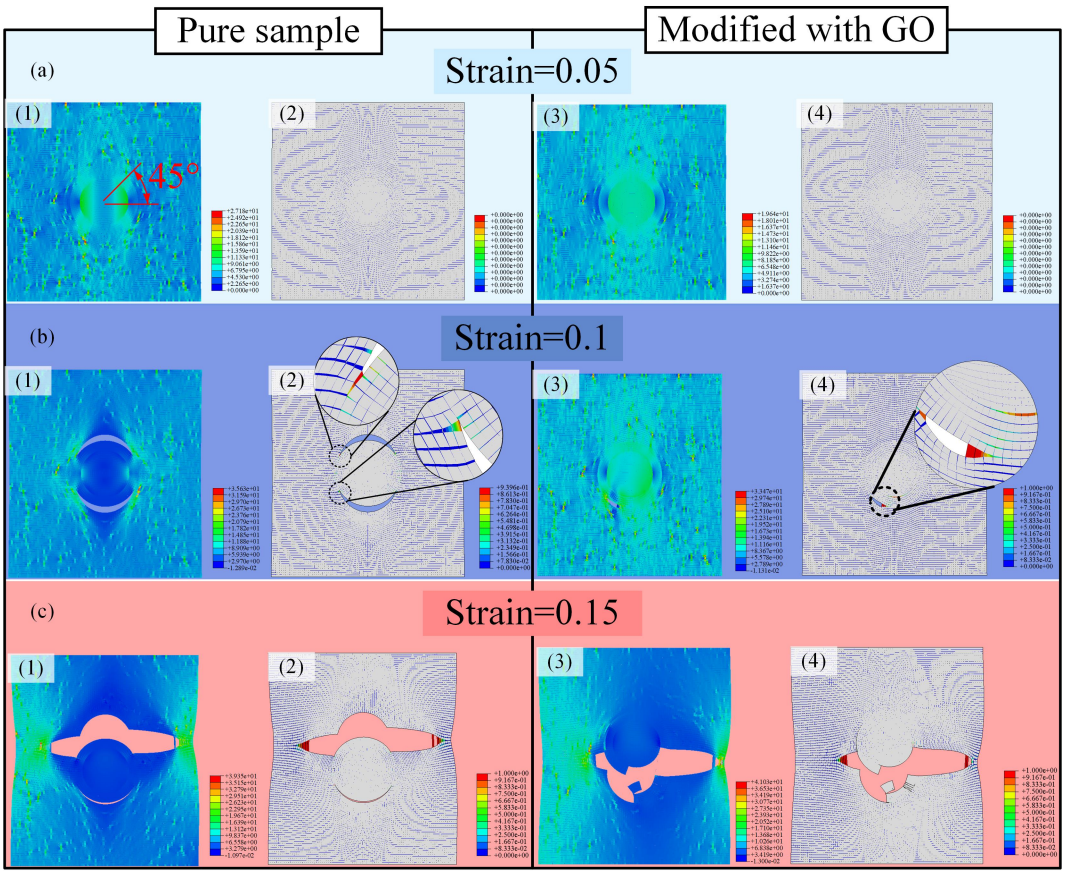

Figure 13: Stress distribution and damage status of the representative volume element model at strain = (a) 0.01, (b) 0.02, and (c) 0.03.

into the matrix at a angle of 45°, in the ITZ region of the pure sample. However, in the GO-modified ITZ sample, the concentration of stress is not obvious in the

ITZ region, and the stress is transmitted almost throughout the model from top to bottom along the high stiffness aggregate particle. It suggests that the addition of GO reduces the stiffness gap between ITZ and aggregate, allowing for more homogeneous distribution of stress [14, 15, 27]. As can be observed from the enlarged view in Fig. 13 (b), at a strain of 0.1, the upper and lower surfaces of the aggregate in the pure sample have been cracked extensively and the cracks start to penetrate into the matrix. At the same time, the GO-reinforced ITZ sample only exhibits brand-new cracks in the ITZ.

At the strain of 0.15, both the pure sample and the GO-modified sample are on the brink of full fracture. It is clear that the pure sample really cracks along the 45° angle of stress concentration in the ITZ, and expands into the matrix along the left and right sides of the horizontal direction simultaneously until it penetrates the whole model. In contrast, the lower surface of the aggregate in the GO-modified ITZ sample exhibits damage throughout the entire ITZ, and the horizontal crack expansion in the matrix lags behind that of the pure sample. The ITZ no longer neatly cracks along the contact surface with the matrix or aggregate, but instead assumes a portion of the resistance to crack expansion. This crack path through the ITZ indicates that GO does enhance the ITZ's fracture toughness. The increased tensile strength and maximum strain of the GO-modified samples are a result of ITZ's enhanced toughness. The global stress-strain curve of single-aggregate model in Fig. 14 (a) shows that the stress of pure sample suddenly decreases when the strain reaches 0.075. It then continues to rise until it reaches the maximum stress (22 MPa) at strain of 0.133, followed by significant brittle damage and finally complete fracture at strain of 0.156. The GO-reinforced ITZ sample, on the other hand, exhibits a higher tensile elasticity modulus(234 MPa), a higher peak stress (27 MPa), and a higher maximum strain (0.17). It's worth mentioning that the "global stress-strain" in this study means the value of force applied on the loaded reference point divided by the cross-sectional area of the model, and the displacement of the reference point divided by the side length of the model.

In the multi aggregate concrete model, the maximum strain substantially decreases and the global stress-strain response becomes more brittle (see Fig. 14 (b)) due to the significant increase in the volume ratio of aggregates and ITZ [91]. As the volume fraction reaches a critical value, the strength of concrete decreases with increasing volume fraction, which is related to the weak adhesion between the aggregate and the matrix [92, 93]. A higher aggregate volume fraction means there will be more aggregate-matrix interfaces, which have a large number of pores and microcracks [94]. And fine aggregates' absorption of surrounding wa-

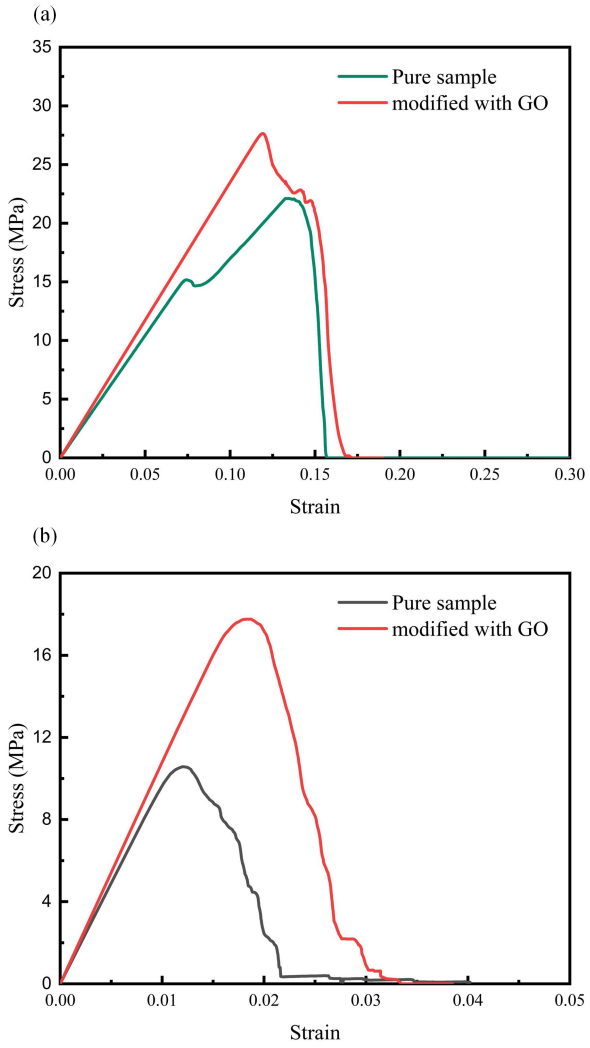

Figure 14: Stress-strain curves of (a) the representative volume element FEM model and (b) the multi aggregate concrete FEM model.

ter may negatively affect the mechanical bonding at the interfacial transition zone [95]. In Fig. 15 the stress distribution and damage evolution results at strains of 0.01, 0.02, and 0.03 are chosen and compared. The pure concrete sample without GO modification exhibits noticeable stress concentration around the aggregate particles under tension. The low stress zones in the core of the aggregates indicate that the sudden change in stiffness and strength near the aggregates hinder

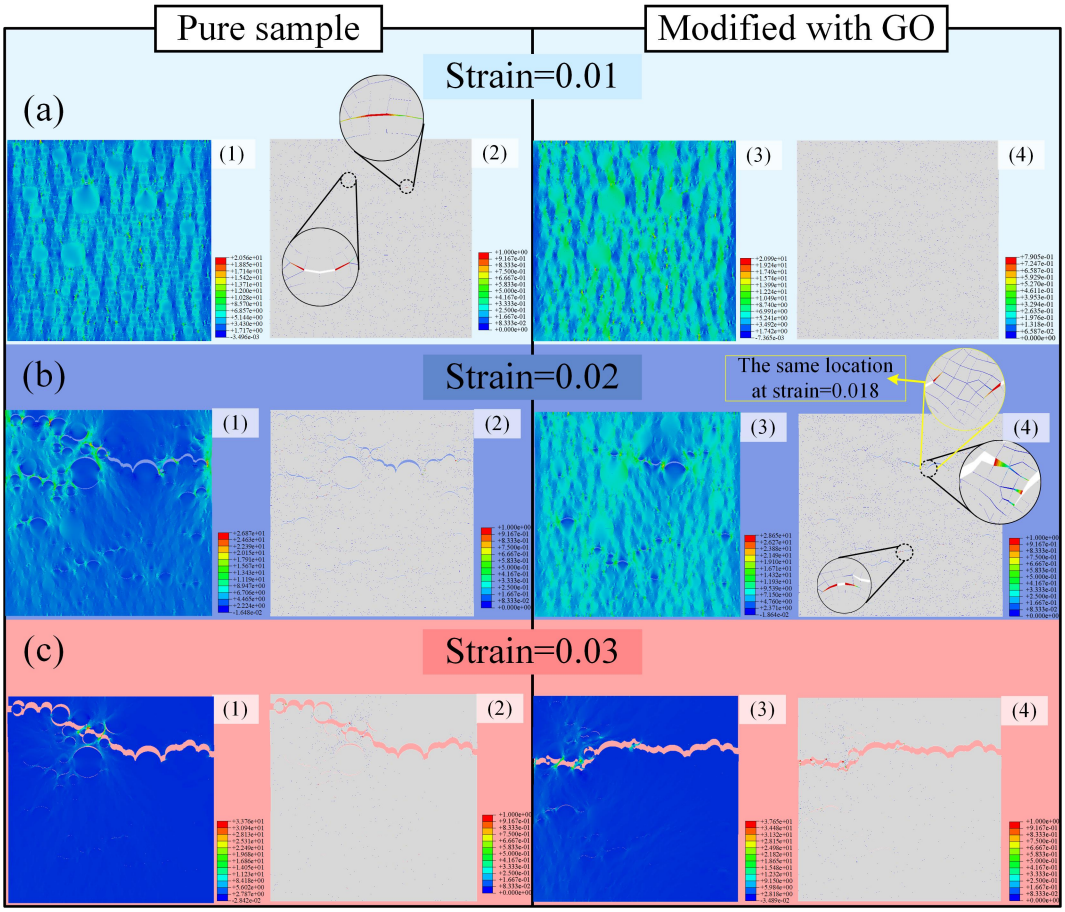

Figure 15: Stress distribution and damage status of the multi aggregate concrete FEM model at strain = (a) 0.05, (b) 0.1, and (c) 0.15.

the transmission of stress, due to the poor mechanical properties of ITZ. The pure concrete sample shows tiny amounts of localized elements' failure, even at a low strain of 0.01 (see Fig. 15 (a1, a2)), but this does not seem to be sufficient to cause an overall stress drop [96] (the peak stress (10 MPa) is reached latter at a strain of 0.012). In contrast, the stresses are more effectively transmitted between the aggregates in the GO-reinforced concrete model, leading to numerous stress bands that run parallel to the axis of the strain. At a strain of 0.01 (Fig. 15 (a3, a4)), a very tiny portion of the elements exhibited stiffness degradation, but no initial cracks were formed. When the strain reaches 0.02, the stress in the pure concrete sample has decreased to 34.75% of the maximum strength, and it is al-

most entirely concentrated in the ITZ near the existing cracks, see Fig. 15 (b1). In Fig. 15 (c1) we can see that, the value of stress in the region away from the cracks is extremely low or even close to zero. Massive cracks were first formed around all the aggregates with large particle sizes ($d \geq 10mm$), and gradually extended to other adjacent aggregate surfaces to form continuous cracks through the model (see Fig. 15 (c1, c3)). The strain in the GO-modified concrete model was 0.018 when the stress reached its peak (18 MPa), the cracks just started to form on the upper and lower surfaces of the aggregates, as shown in enlarged view of damage status in Fig. 15 (b4). The extensive stress concentration region at the end of cracks implies that the GO-reinforced ITZ has a considerable blunting impact on the crack tips [97], and the crack therefore has not yet penetrated into the matrix to form continuous cracks going through multiple aggregates [98]. Both pure and GO-modified concrete models were on the verge of complete damage at a strain of 0.03. In contrast to the pure concrete model, the cracks in the GO-modified concrete model took a different path, and as shown in Fig. 15 (c), the GO-modified concrete samples still had quite a bit of ITZ and matrix attached to the sides of the cracks after the cracks penetrated the entire section. These adherent regions improved the toughness of the GO-modified concrete sample, allowing a larger maximum strain than the pure concrete model (as shown in Fig. 14 (b)).

4. Conclusions

In this paper, a multiscale model of cementitious composites considering ITZ was constructed by molecular dynamics simulation and finite element method. The fracture mechanical properties of different phases (C-S-H, CH, quartz, and GO) and their interfacial composites were investigated. The bottom-up design of concrete materials was attempted by exploring the enhancement of GO on ITZ utilizing the key parameters of nanostructures as input parameters of the finite element model.

The fracture toughness and energy release rates of matrix, ITZ, and aggregate at nanoscale was determined by molecular dynamics simulation. The energy release rate of the ITZ structure decreased to $6.41\% \sim 9.94\%$ of C-S-H and CH due to the poor interfacial bonding between the different phases. By adding GO sheets into the interface, the ITZ system's fracture toughness was increased by $38.40\% \sim 58.06\%$. The better plastic deformation capacity of the GO-modified ITZ structure is primarily attributed to the atomic interaction between the Ca atoms and oxygen-containing functional groups on the GO sheet and the hydrogen bonds in the interface.

In both single-aggregate and multi-aggregate finite element models, GO-modified ITZ resulted in more uniform stress transmission near the aggregates, as well as wider and more continuous stress bands along the strain direction. In the case of continuous cracks generated between aggregate particles, the GO-modified ITZ was effective in delaying the crack extension into the matrix and forming a blunting region at the crack tips. The GO-modified concrete model showed an 80% increase in tensile strength and a 9.81% increase in tensile modulus.

These findings highlight the potential of using nanoscale design to optimize the mechanical properties of cementitious composites, particularly through the incorporation of GO into the ITZ. This study provides valuable insights into the bottom-up design of concrete materials and paves the way for future research on the development of advanced cementitious composites with enhanced mechanical properties for a wide range of applications.

Acknowledgement

This work was supported by the National Natural Science Foundation of China with Grant NO. 11532013 and 11872157. The authors gratefully acknowledge financial support from China Scholarship Council. We would like to acknowledge computing support from National Supercomputing Centre Singapore (NSCC), and force field support from Materials Computation Center of Penn State University.

References

[1] P. J. M. Monteiro, S. A. Miller, A. Horvath, Towards sustainable concrete, Nature Materials 16 (7) (2017) 698–699. doi:{10.1038/nmat4930}.

[2] K. Daehn, R. Basuhi, J. Gregory, M. Berlinger, V. Somjit, E. A. Olivetti, Innovations to decarbonize materials industries, Nature Reviews Materials 2021 7:4 7 (2021) 275–294. doi:10.1038/s41578-021-00376-y. URL https://www.nature.com/articles/s41578-021-00376-y

[3] M. Peplow, The race to upcycle co2 into fuels, concrete and more, Nature 603 (2022) 780–783. doi:10.1038/D41586-022-00807-Y.

[4] L. Chi, S. Lu, Y. Yao, Damping additives used in cement-matrix composites: A review, Composites Part B: Engineering 164 (2019) 26–36. doi:https://doi.org/10.1016/j.compositesb.2018.11.057.

URL https://www.sciencedirect.com/science/article/pii/S1359836818311259

[5] M. Jalal, E. Teimortashlu, Z. Grasley, Performance-based design and optimization of rheological and strength properties of self-compacting cement composite incorporating micro/ nano admixtures, Composites Part B: Engineering 163 (2019) 497–510. doi:https://doi.org/10.1016/j.compositesb.2019.01.028.
URL https://www.sciencedirect.com/science/article/pii/S1359836818319826

[6] V. Corinaldesi, A. Nardinocchi, Mechanical characterization of engineered cement-based composites prepared with hybrid fibres and expansive agent, Composites Part B: Engineering 98 (2016) 389–396. doi:https://doi.org/10.1016/j.compositesb.2016.05.051.
URL https://www.sciencedirect.com/science/article/pii/S1359836816307417

[7] W. Zhang, Q. Zheng, A. Ashour, B. Han, Self-healing cement concrete composites for resilient infrastructures: A review, Composites Part B-Engineering 189 (MAY 15 2020). doi:10.1016/j.compositesb.2020.107892.

[8] J. Li, Z. Wu, C. Shi, Q. Yuan, Z. Zhang, Durability of ultra-high performance concrete – a review, Construction and Building Materials 255 (2020) 119296. doi:https://doi.org/10.1016/j.conbuildmat.2020.119296.
URL https://www.sciencedirect.com/science/article/pii/S0950061820313015

[9] J. An, B. H. Nam, Y. Alharbi, B. H. Cho, M. Khawaji, Edge-oxidized graphene oxide (eogo) in cement composites: Cement hydration and microstructure, Composites Part B: Engineering 173 (2019) 106795. doi:https://doi.org/10.1016/j.compositesb.2019.05.006.
URL https://www.sciencedirect.com/science/article/pii/S1359836818329998

[10] Y. Zheng, Y. Zhang, J. Zhuo, Y. Zhang, C. Wan, A review of the mechanical properties and durability of basalt fiber-reinforced concrete, Construction and Building Materials 359 (2022) 129360. doi:https://doi.org/

10.1016/j.conbuildmat.2022.129360.
URL https://www.sciencedirect.com/science/article/pii/S0950061822030161

[11] K. Liew, A. Akbar, The recent progress of recycled steel fiber reinforced concrete, Construction and Building Materials 232 (2020) 117232. doi:https://doi.org/10.1016/j.conbuildmat.2019.117232.
URL https://www.sciencedirect.com/science/article/pii/S0950061819326844

[12] H. Khalel, M. Khan, A. Starr, K. A. Khan, A. Muhammad, Performance of engineered fibre reinforced concrete (efrc) under different load regimes: A review, Construction and Building Materials 306 (2021) 124692. doi:https://doi.org/10.1016/j.conbuildmat.2021.124692.
URL https://www.sciencedirect.com/science/article/pii/S0950061821024478

[13] F. Aslani, J. Kelin, Assessment and development of high-performance fibre-reinforced lightweight self-compacting concrete including recycled crumb rubber aggregates exposed to elevated temperatures, Journal of Cleaner Production 200 (2018) 1009–1025. doi:https://doi.org/10.1016/j.jclepro.2018.07.323.
URL https://www.sciencedirect.com/science/article/pii/S0959652618323187

[14] S. Pirmohammad, Y. Majd Shokorlou, B. Amani, Laboratory investigations on fracture toughness of asphalt concretes reinforced with carbon and kenaf fibers, Engineering Fracture Mechanics 226 (2020) 106875. doi:https://doi.org/10.1016/j.engfracmech.2020.106875.
URL https://www.sciencedirect.com/science/article/pii/S0013794419309920

[15] M. Monazami, R. Gupta, Investigation of mechanical behavior and fracture energy of fiber-reinforced concrete beams and panels, Cement and Concrete Composites 133 (2022) 104656. doi:https://doi.org/10.1016/j.cemconcomp.2022.104656.
URL https://www.sciencedirect.com/science/article/pii/S0958946522002499

[16] M. Aliha, H. reza Karimi, M. Abedi, The role of mix design and short glass fiber content on mode-i cracking characteristics of polymer concrete, Construction and Building Materials 317 (2022) 126139. doi:https://doi.org/10.1016/j.conbuildmat.2021.126139.
URL https://www.sciencedirect.com/science/article/pii/S095006182103871X

[17] D. Zhu, S. Liu, Y. Yao, G. Li, Y. Du, C. Shi, Effects of short fiber and pretension on the tensile behavior of basalt textile reinforced concrete, Cement and Concrete Composites 96 (2019) 33–45. doi:https://doi.org/10.1016/j.cemconcomp.2018.11.015.
URL https://www.sciencedirect.com/science/article/pii/S0958946518300921

[18] C. Xie, M. Cao, M. Khan, H. Yin, J. Guan, Review on different testing methods and factors affecting fracture properties of fiber reinforced cementitious composites, Construction and Building Materials 273 (2021) 121766. doi:https://doi.org/10.1016/j.conbuildmat.2020.121766.
URL https://www.sciencedirect.com/science/article/pii/S0950061820337703

[19] Y. Gan, H. Zhang, M. Liang, Y. Zhang, E. Schlangen, K. van Breugel, B. Šavija, Flexural strength and fatigue properties of interfacial transition zone at the microscale, Cement and Concrete Composites 133 (2022) 104717. doi:https://doi.org/10.1016/j.cemconcomp.2022.104717.
URL https://www.sciencedirect.com/science/article/pii/S0958946522003109

[20] D. Hou, Z. Lu, X. Li, H. Ma, Z. Li, Reactive molecular dynamics and experimental study of graphene-cement composites: Structure, dynamics and reinforcement mechanisms, Carbon 115 (2017) 188–208. doi:https://doi.org/10.1016/j.carbon.2017.01.013.
URL https://www.sciencedirect.com/science/article/pii/S0008622317300234

[21] T. Liang, Y. Lai, D. Hou, W. Pei, M. Wang, F. Yu, Q. Yang, Y. Yang, H. Li, Molecular dynamics simulation investigation on the anti-freezing mechanisms of csh-gs/go interfaces, Construction and Building Materials 369 (2023) 130581. doi:https://doi.org/10.1016/j.

conbuildmat.2023.130581.
URL https://www.sciencedirect.com/science/article/pii/S0950061823002921

[22] C. Wu, D. Hou, B. Yin, S. Li, Synthesis and application of new core-shell structure via pickering emulsion polymerization stabilized by graphene oxide, Composites Part B: Engineering 247 (2022) 110285. doi:https://doi.org/10.1016/j.compositesb.2022.110285.
URL https://www.sciencedirect.com/science/article/pii/S1359836822006588

[23] M. Cao, C. Xie, J. Guan, Fracture behavior of cement mortar reinforced by hybrid composite fiber consisting of caco3 whiskers and pva-steel hybrid fibers, Composites Part A: Applied Science and Manufacturing 120 (2019) 172–187. doi:https://doi.org/10.1016/j.compositesa.2019.03.002.
URL https://www.sciencedirect.com/science/article/pii/S1359835X19300752

[24] J. Feng, F. Yang, S. Qian, Improving the bond between polypropylene fiber and cement matrix by nano calcium carbonate modification, Construction and Building Materials 269 (2021) 121249. doi:https://doi.org/10.1016/j.conbuildmat.2020.121249.
URL https://www.sciencedirect.com/science/article/pii/S0950061820332530

[25] Y. Liu, C. Shi, Z. Zhang, N. Li, D. Shi, Mechanical and fracture properties of ultra-high performance geopolymer concrete: Effects of steel fiber and silica fume, Cement and Concrete Composites 112 (2020) 103665. doi:https://doi.org/10.1016/j.cemconcomp.2020.103665.
URL https://www.sciencedirect.com/science/article/pii/S0958946520301578

[26] L. Yu, S. Bai, X. Guan, Effect of graphene oxide on microstructure and micromechanical property of ultra-high performance concrete, Cement and Concrete Composites 138 (2023) 104964. doi:https://doi.org/10.1016/j.cemconcomp.2023.104964.
URL https://www.sciencedirect.com/science/article/pii/S0958946523000380

[27] S. Guo, Y. Lu, X. Wan, F. Wu, T. Zhao, C. Shen, Preparation, characterization of highly dispersed reduced graphene oxide/epoxy resin and its application in alkali-activated slag composites, Cement and Concrete Composites 105 (2020) 103424. doi:https://doi.org/10.1016/j.cemconcomp.2019.103424.
URL https://www.sciencedirect.com/science/article/pii/S0958946519307607

[28] J. Liu, J. Fu, T. Ni, Y. Yang, Fracture toughness improvement of multi-wall carbon nanotubes/graphene sheets reinforced cement paste, Construction and Building Materials 200 (2019) 530–538. doi:https://doi.org/10.1016/j.conbuildmat.2018.12.141.
URL https://www.sciencedirect.com/science/article/pii/S0950061818331301

[29] Q. Fu, Z. Zhou, Z. Wang, J. Huang, D. Niu, Insight into dynamic compressive response of carbon nanotube/carbon fiber-reinforced concrete, Cement and Concrete Composites 129 (2022) 104471. doi:https://doi.org/10.1016/j.cemconcomp.2022.104471.
URL https://www.sciencedirect.com/science/article/pii/S095894652200066X

[30] S. Xu, Y. Lyu, S. Xu, Q. Li, Enhancing the initial cracking fracture toughness of steel-polyvinyl alcohol hybrid fibers ultra high toughness cementitious composites by incorporating multi-walled carbon nanotubes, Construction and Building Materials 195 (2019) 269–282. doi:https://doi.org/10.1016/j.conbuildmat.2018.10.133.
URL https://www.sciencedirect.com/science/article/pii/S0950061818325443

[31] J. Chen, A.-T. Akono, Influence of multi-walled carbon nanotubes on the hydration products of ordinary portland cement paste, Cement and Concrete Research 137 (2020) 106197. doi:https://doi.org/10.1016/j.cemconres.2020.106197.
URL https://www.sciencedirect.com/science/article/pii/S0008884620304671

[32] O. A. Hisseine, A. Tagnit-Hamou, Nanocellulose for ecological nanoengineered strain-hardening cementitious composites incorporating

high-volume ground-glass pozzolans, Cement and Concrete Composites 112 (2020) 103662. doi:https://doi.org/10.1016/j.cemconcomp.2020.103662.
URL https://www.sciencedirect.com/science/article/pii/S0958946520301542

[33] N. Tourani, K. Sagoe-Crentsil, W. Duan, Strain-rate-dependent performance of cementitious nanocomposites: Nanosilica and the role of dispersion, Cement and Concrete Research 161 (2022) 106966. doi:https://doi.org/10.1016/j.cemconres.2022.106966.
URL https://www.sciencedirect.com/science/article/pii/S0008884622002587

[34] P. Zhang, K. Wang, J. Wang, J. Guo, S. Hu, Y. Ling, Mechanical properties and prediction of fracture parameters of geopolymer/alkali-activated mortar modified with pva fiber and nano-sio2, Ceramics International 46 (12) (2020) 20027–20037. doi:https://doi.org/10.1016/j.ceramint.2020.05.074.
URL https://www.sciencedirect.com/science/article/pii/S0272884220313626

[35] Y. Yang, Q. Zhou, Y. Deng, J. Lin, Reinforcement effects of multi-scale hybrid fiber on flexural and fracture behaviors of ultra-low-weight foamed cement-based composites, Cement and Concrete Composites 128 (2022) 104422. doi:https://doi.org/10.1016/j.cemconcomp.2022.104422.
URL https://www.sciencedirect.com/science/article/pii/S095894652200018X

[36] M. Congro, E. C. M. Sanchez, D. Roehl, E. Marangon, Fracture modeling of fiber reinforced concrete in a multiscale approach, Composites Part B: Engineering 174 (2019) 106958. doi:https://doi.org/10.1016/j.compositesb.2019.106958.
URL https://www.sciencedirect.com/science/article/pii/S1359836819310285

[37] F. Mukhtar, A. El-Tohfa, A review on fracture propagation in concrete: Models, methods, and benchmark tests, Engineering Fracture Mechanics 281 (2023) 109100. doi:https://doi.org/10.1016/j.

engfracmech.2023.109100.
URL https://www.sciencedirect.com/science/article/pii/S0013794423000589

[38] D. Wei, R. C. Hurley, L. H. Poh, D. D. da Costa, Y. Gan, The role of particle morphology on concrete fracture behaviour: A meso-scale modelling approach, Cement and Concrete Research 134 (2020) 106096. doi:https://doi.org/10.1016/j.cemconres.2020.106096.
URL https://www.sciencedirect.com/science/article/pii/S0008884620301587

[39] M. Hlobil, K. Sotiriadis, A. Hlobilová, Scaling of strength in hardened cement pastes - unveiling the role of microstructural defects and the susceptibility of c-s-h gel to physical/chemical degradation by multiscale modeling, Cement and Concrete Research 154 (2022) 106714. doi:https://doi.org/10.1016/j.cemconres.2022.106714.
URL https://www.sciencedirect.com/science/article/pii/S0008884622000059

[40] Y. Chen, X. Han, X. Hu, Q. Li, Design of concrete fracture property by average aggregate size, Cement and Concrete Composites 122 (2021) 104105. doi:https://doi.org/10.1016/j.cemconcomp.2021.104105.
URL https://www.sciencedirect.com/science/article/pii/S0958946521001748

[41] H. Zhang, Y. Xu, Y. Gan, E. Schlangen, B. Šavija, Experimentally validated meso-scale fracture modelling of mortar using output from micromechanical models, Cement and Concrete Composites 110 (2020) 103567. doi:https://doi.org/10.1016/j.cemconcomp.2020.103567.
URL https://www.sciencedirect.com/science/article/pii/S0958946520300597

[42] M. S. Konsta-Gdoutos, Z. S. Metaxa, S. P. Shah, Multi-scale mechanical and fracture characteristics and early-age strain capacity of high performance carbon nanotube/cement nanocomposites, Cement and Concrete Composites 32 (2) (2010) 110–115. doi:https://doi.org/10.1016/j.cemconcomp.2009.10.007.
URL https://www.sciencedirect.com/science/article/pii/S0958946509001632

[43] K. Ragalwar, W. F. Heard, B. A. Williams, D. Kumar, R. Ranade, On enhancing the mechanical behavior of ultra-high performance concrete through multi-scale fiber reinforcement, Cement and Concrete Composites 105 (2020) 103422. doi:https://doi.org/10.1016/j.cemconcomp.2019.103422.
URL https://www.sciencedirect.com/science/article/pii/S0958946519307309

[44] M. Liu, P. Qiao, L. Sun, Dependence of chloride ion diffusivity on evolution of pore-structures in freeze-thawed shotcrete: Multiscale characterization and modeling, Cement and Concrete Composites 123 (2021) 104222. doi:https://doi.org/10.1016/j.cemconcomp.2021.104222.
URL https://www.sciencedirect.com/science/article/pii/S0958946521002900

[45] S. Nayak, N. A. Krishnan, S. Das, Fracture response of metallic particulate-reinforced cementitious composites: Insights from experiments and multiscale numerical simulations, Cement and Concrete Composites 97 (2019) 154–165. doi:https://doi.org/10.1016/j.cemconcomp.2018.12.026.
URL https://www.sciencedirect.com/science/article/pii/S0958946518310382

[46] S. Hamid, The crystal structure of the 11å natural tobermorite ca2. 25 [si3o7. 5 (oh) 1.5]· 1h2o, Zeitschrift für Kristallographie-Crystalline Materials 154 (3-4) (1981) 189–198. doi:10.1524/zkri.1981.154.14.189.

[47] I. Richardson, The nature of c-s-h in hardened cements, Cement and Concrete Research 29 (8) (1999) 1131–1147. doi:10.1016/S0008-8846(99)00168-4.

[48] A. Ayuela, J. S. Dolado, I. Campillo, Y. De Miguel, E. Erkizia, D. Sánchez-Portal, A. Rubio, A. Porro, P. M. Echenique, Silicate chain formation in the nanostructure of cement-based materials, The Journal of chemical physics 127 (16) (2007) 164710. doi:10.1063/1.2796171.

[49] M. Benzhi, W. Pengyu, L. Shuzhou, W. Zhenqing, Mechanical influence of graphene oxide in the interface between calcium silicate hydrate and quartz: A molecular dynamics study, Construction and Building Materials 325 (MAR 28 2022). doi:10.1016/j.conbuildmat.2022.126597.

[50] Y. Gao, X. Zhu, D. J. Corr, M. S. Konsta-Gdoutos, S. P. Shah, Characterization of the interfacial transition zone of cnf-reinforced cementitious composites, Cement and Concrete Composites 99 (2019) 130–139. doi:10.1016/j.cemconcomp.2019.03.002.

[51] R. S. Teixeira, G. H. D. Tonoli, S. F. Santos, E. Rayon, V. Amigo, H. Savastano, Jr., F. A. Rocco Lahr, Nanoindentation study of the interfacial zone between cellulose fiber and cement matrix in extruded composites, Cement and Concrete Composites 85 (2018) 1–8. doi:10.1016/j.cemconcomp.2017.09.018.

[52] K. Scrivener, A. Crumbie, P. Laugesen, The interfacial transition zone (itz) between cement paste and aggregate in concrete, Interface Science 12 (4) (2004) 411–421. doi:10.1023/B:INTS.0000042339.92990.4c.

[53] W. R. Busing, H. A. Levy, Neutron diffraction study of calcium hydroxide, The Journal of Chemical Physics 26 (1957) 563–568. doi:10.1063/1.1743345.

[54] S. Plimpton, Fast parallel algorithms for short-range molecular dynamics, Journal of computational physics 117 (1) (1995) 1–19. doi:10.2172/10176421.

[55] H. Manzano, S. Moeini, F. Marinelli, A. C. T. van Duin, F.-J. Ulm, R. J. M. Pellenq, Confined water dissociation in microporous defective silicates: Mechanism, dipole distribution, and impact on substrate properties, Journal of the American Chemical Society 134 (4) (2012) 2208–2215. doi:10.1021/ja209152n.

[56] R. Cygan, J. Liang, A. Kalinichev, Molecular models of hydroxide, oxyhydroxide, and clay phases and the development of a general force field, Journal of Physical Chemistry B 108 (4) (2004) 1255–1266. doi:10.1021/jp0363287.

[57] R. T. Cygan, J. A. Greathouse, A. G. Kalinichev, Advances in clayff molecular simulation of layered and nanoporous materials and their aqueous interfaces, The Journal of Physical Chemistry C 125 (32) (2021) 17573–17589. doi:10.1021/acs.jpcc.1c04600.

[58] S. Zhu, M. A. Khan, T. Kameda, H. Xu, F. Wang, M. Xia, T. Yoshioka, New insights into the capture performance and mechanism of hazardous metals

cr3+ and cd2+ onto an effective layered double hydroxide based material, Journal of Hazardous Materials 426 (MAR 15 2022). doi:10.1016/j.jhazmat.2021.128062.

[59] X. Wang, W. Liu, W. Liu, Y. Shen, H. Duan, J. Qiu, X. Gu, Understanding adsorption of amine surfactants on the solvated quartz (101) surface by a jointed dreiding-clayff force field, Applied Surface Science 566 (NOV 15 2021). doi:10.1016/j.apsusc.2021.150737.

[60] J. Fu, S. Kamali-Bernard, F. Bernard, M. Cornen, Comparison of mechanical properties of c-s-h and portlandite between nano-indentation experiments and a modeling approach using various simulation techniques, Composites Part B: Engineering 151 (2018) 127–138. doi:10.1016/j.compositesb.2018.05.043.

[61] P. Dauber-Osguthorpe, V. A. Roberts, D. J. Osguthorpe, J. Wolff, M. Genest, A. T. Hagler, Structure and energetics of ligand binding to proteins: Escherichia coli dihydrofolate reductase-trimethoprim, a drug-receptor system, Proteins: Structure, Function, and Bioinformatics 4 (1) (1988) 31–47. doi:10.1002/prot.340040106.

[62] F. Sanchez, L. Zhang, Interaction energies, structure, and dynamics at functionalized graphitic structure–liquid phase interfaces in an aqueous calcium sulfate solution by molecular dynamics simulation, Carbon 48 (4) (2010) 1210–1223. doi:10.1016/j.carbon.2009.11.044.

[63] M. P. Allen, D. J. Tildesley, Computer Simulation of Liquids, Oxford University Press, 2017. doi:10.1093/oso/9780198803195.001.0001.
URL https://doi.org/10.1093/oso/9780198803195.001.0001

[64] T. Lu, F. Chen, Multiwfn: A multifunctional wavefunction analyzer, Journal of Computational Chemistry 33 (5) (2012) 580–592. arXiv:https://onlinelibrary.wiley.com/doi/pdf/10.1002/jcc.22885, doi:https://doi.org/10.1002/jcc.22885.

[65] M. Bauchy, H. Laubie, M. J. A. Qomi, C. G. Hoover, F. J. Ulm, R. J. M. Pellenq, Fracture toughness of calcium-silicate-hydrate from molecular dy-

namics simulations, Journal of Non-crystalline Solids 419 (2015) 58–64. doi:10.1016/j.jnoncrysol.2015.03.031.

[66] Y. Zhang, S. Zhang, X. Jiang, Q. Chen, Z. Jiang, J. W. Ju, M. Bauchy, Insights into the thermal effect on the fracture toughness of calcium silicate hydrate grains: A reactive molecular dynamics study, Cement and Concrete Composites 134 (2022) 104824. doi:https://doi.org/10.1016/j.cemconcomp.2022.104824.
URL https://www.sciencedirect.com/science/article/pii/S0958946522004176

[67] N. Zhang, R. Shahsavari, Balancing strength and toughness of calcium-silicate-hydrate via random nanovoids and particle inclusions: Atomistic modeling and statistical analysis, Journal of the Mechanics and Physics of Solids 96 (2016) 204–222. doi:https://doi.org/10.1016/j.jmps.2016.07.021.

[68] D. Chung, W. Buessem, The voigt-reuss-hill approximation and elastic moduli of polycrystalline mgo, caf2, β-zns, znse, and cdte, Journal of Applied Physics 38 (6) (1967) 2535–2540.

[69] D. Hou, T. Yang, A reactive molecular dynamics study of graphene oxide sheets in different saturated states: structure, reactivity and mechanical properties, Physical Chemistry Chemical Physics 20 (16) (2018) 11053–11066. doi:10.1039/c8cp00813b.

[70] J. J. Thomas, J. J. Biernacki, J. W. Bullard, S. Bishnoi, J. S. Dolado, G. W. Scherer, A. Luttge, Modeling and simulation of cement hydration kinetics and microstructure development, Cement and Concrete Research 41 (12, SI) (2011) 1257–1278. doi:10.1016/j.cemconres.2010.10.004.

[71] D. Hou, H. Li, L. Zhang, J. Zhang, Nano-scale mechanical properties investigation of c-s-h from hydrated tri-calcium silicate by nano-indentation and molecular dynamics simulation, Construction and Building Materials 189 (2018) 265–275. doi:https://doi.org/10.1016/j.conbuildmat.2018.08.215.
URL https://www.sciencedirect.com/science/article/pii/S0950061818321561

[72] F. Ulm, G. Constantinides, F. Heukamp, Is concrete a poromechanics material? - a multiscale investigation of poroelastic properties, Materials and Structures 37 (265) (2004) 43–58. doi:10.1007/BF02481626.

[73] S.-M. Kim, R. K. Abu Al-Rub, Meso-scale computational modeling of the plastic-damage response of cementitious composites, Cement and Concrete Research 41 (3) (2011) 339–358. doi:10.1016/j.cemconres.2010.12.002.

[74] M. Eftekhari, S. Mohammadi, M. Khanmohammadi, A hierarchical nano to macro multiscale analysis of monotonic behavior of concrete columns made of cnt-reinforced cement composite, Construction and Building Materials 175 (2018) 134–143. doi:10.1016/j.conbuildmat.2018.04.168.

[75] T. Mori, K. Tanaka, Average stress in matrix and average elastic energy of materials with misfitting inclusions, Acta Metallurgica 21 (5) (1973) 571–574. doi:https://doi.org/10.1016/0001-6160(73)90064-3.
URL https://www.sciencedirect.com/science/article/pii/0001616073900643

[76] C. Helimich, H. Mang, Shotcrete elasticity revisited in the framework of continuum micromechanics: From submicron to meter level, Journal of Materials in Civil Engineering 17 (3) (2005) 246–256. doi:10.1061/(ASCE)0899-1561(2005)17:3(246).

[77] G. Constantinides, F.-J. Ulm, The effect of two types of c-s-h on the elasticity of cement-based materials: Results from nanoindentation and micromechanical modeling, Cement and Concrete Research 34 (1) (2004) 67–80. doi:https://doi.org/10.1016/S0008-8846(03)00230-8.

[78] B. Pichler, C. Hellmich, J. Eberhardsteiner, Spherical and acicular representation of hydrates in a micromechanical model for cement paste: prediction of early-age elasticity and strength, ACTA MECHANICA 203 (3-4) (2009) 137–162. doi:10.1007/s00707-008-0007-9.

[79] W. Wu, J. Owino, A. Al-Ostaz, L. Cai, Applying periodic boundary conditions in finite element analysis, in: Simulia Community Conference, 2014, pp. 707–719.

[80] D. J. Walters, D. J. Luscher, J. D. Yeager, Considering computational speed vs. accuracy: Choosing appropriate mesoscale rve boundary conditions, Computer Methods in Applied Mechanics and Engineering 374 (FEB 1 2021). doi:10.1016/j.cma.2020.113572.

[81] S. L. Omairey, P. D. Dunning, S. Sriramula, Development of an abaqus plugin tool for periodic rve homogenisation, Engineering with Computers 35 (2) (2019) 567–577. doi:10.1007/s00366-018-0616-4.

[82] Z. Xia, Y. Zhang, F. Ellyin, A unified periodical boundary conditions for representative volume elements of composites and applications, International Journal of Solids and Structures 40 (8) (2003) 1907–1921. doi:10.1016/S0020-7683(03)00024-6.

[83] T. Namikawa, J. Koseki, Evaluation of tensile strength of cement-treated sand based on several types of laboratory tests, Soils and Foundations 47 (4) (2007) 657–674. doi:10.3208/sandf.47.657.

[84] X. Chen, S. Wu, J. Zhou, Influence of porosity on compressive and tensile strength of cement mortar, Construction and Building Materials 40 (2013) 869–874. doi:10.1016/j.conbuildmat.2012.11.072.

[85] X. Chen, S. Wu, J. Zhou, Experimental study on dynamic tensile strength of cement mortar using split hopkinson pressure bar technique, Journal of Materials in Civil Engineering 26 (6) (JUN 2014). doi:10.1061/(ASCE)MT.1943-5533.0000926.

[86] Y. Li, J. Li, Relationship between fracture area and tensile strength of cement paste with supplementary cementitious materials, Construction and Building Materials 79 (2015) 223–228. doi:10.1016/j.conbuildmat.2015.01.052.

[87] S. Singh, P. Munjal, N. Thammishetti, Role of water/cement ratio on strength development of cement mortar, Journal of Building Engineering 4 (2015) 94–100. doi:https://doi.org/10.1016/j.jobe.2015.09.003.
URL https://www.sciencedirect.com/science/article/pii/S2352710215300231